

Combining underground and on-surface third-generation gravitational-wave interferometers

Francesco Iacovelli ^{1,2} Enis Belgacem ^{1,2} Michele Maggiore ^{1,2}
Michele Mancarella ³ Niccolò Muttoni ^{1,2}

¹Département de Physique Théorique, Université de Genève, 24 quai Ernest Ansermet, 1211 Genève 4, Switzerland

²Gravitational Wave Science Center (GWSC), Université de Genève, CH-1211 Geneva, Switzerland

³Aix-Marseille Univ., Université de Toulon, CNRS, CPT, Marseille, France

E-mail: Francesco.Iacovelli@unige.ch, Enis.Belgacem@unige.ch,
Michele.Maggiore@unige.ch, mancarella@cpt.univ-mrs.fr,
Niccolo.Muttoni@unige.ch

Abstract. Recently, detailed studies have been made to compare the performance of the European next generation GW observatory Einstein Telescope (ET) in a single-site triangular configuration with the performance of a configuration featuring two L-shaped detectors in different sites, still taken to have all other ET characteristics except for the geometry, in particular, underground and composed of a low-frequency interferometer working at cryogenic temperatures and a high-frequency interferometer working at room temperature. Here we study a further possibility for a European network, made by a single L-shaped underground detector, like one of the detectors considered for the 2L version of ET, and a single third-generation 20-km L-shaped interferometer on the surface. We compare the performances of such a network to those of the triangle and of the 2L-underground ET configurations. We then examine the performance of an intercontinental network made by a 40-km CE in the US, together with any of these European networks.

Contents

1	Introduction	1
2	Detector configurations	2
3	Methodology	5
4	Results	6
4.1	Horizons	6
4.2	Parameter reconstruction of coalescing binaries	8
4.2.1	European networks	8
4.2.2	European networks together with a CE-40km in the US	13
4.3	Pre-merger alerts	18
4.4	Stochastic backgrounds	20
5	Conclusions	28

1 Introduction

The detection of gravitational waves (GWs) in the last few years demonstrated the possibility of a novel way to observe the Universe by “listening” to the ripples of spacetime. The second generation detectors LIGO and Virgo revealed the existence of stellar-scale black holes more massive than expected and neutron-star mergers emitting both GWs and light signals across the entire spectrum, while providing additional confirmation of Einstein’s theory of General Relativity [1–9].

Building on this success, the GW community is preparing the jump toward third-generation (3G) GW detectors, new observatories that overcome the limitations imposed by existing second-generation detector infrastructures and are designed to detect GW sources along the cosmic history up to the early Universe. The Einstein Telescope (ET) [10–12] is the 3G European observatory project, while the US community effort is represented by the Cosmic Explorer (CE) project [13–15]. These detectors will provide an improvement in sensitivity by one order of magnitude and a significant enlargement of the bandwidth, both toward low and high frequencies, and will have extraordinary potential for discoveries in astrophysics, cosmology, and fundamental physics.

In the last few years, comprehensive studies of the scientific potential of various 3G detector networks have been performed [16–18]. In particular, in ref. [17] two different geometries for ET were compared, a single-site triangular geometry made of 3 nested detectors [each comprising two interferometers, a low frequency (LF) and a high-frequency (HF) one, for a total of six nested interferometers], and a network made of two identical L-shaped detectors (“2L” in the following), again made by a LF and a HF interferometer each, located in two different sites within Europe (see also [19–22] for further follow-up studies). These different configurations for ET were considered both in a ET-only scenario, and in a broader world-wide network including also a single 40-km Cosmic Explorer (CE) detector, or two CE detectors with arm-lengths of 20 and 40 km, respectively.

The main aim of the present paper is to investigate the performance of a hypothetical European detector network made by a single L-shaped underground detector with the amplitude spectral density (ASD) of ET and a single 3G L-shaped interferometer on the surface, and compare it with the other 3G detector network configurations that have been recently studied. We will first compare the performances of these configurations taken as European networks in isolation, and we will then further compare their performances when they are part of a broader world-wide network including also a single 40-km Cosmic Explorer (CE) detector in the US.

2 Detector configurations

As discussed in ref. [17], a single-L 3G detector, operated in isolation and not inserted in a network, would miss many of the science goals expected from the next generation of GW detectors. A network of at least two L-shaped 3G detectors with the characteristics of ET would instead allow reaching them [17], as would also be the case for two 3G detectors with the characteristics of CE [15, 18].

Each of these designs, ET or CE, has its own advantages. The ET design allows reaching a better sensitivity at low frequencies, thanks to the cryogenic LF instrument and to the fact that in an underground facility the seismic noise is lower. On the other hand, the fact that CE is not underground allows one to make longer arms (for a given cost), which provide a better sensitivity above about 10 Hz. Figure 1 shows the ASD for a single-L ET (with 10 km arms and with 15 km arms), for CE (with 20-km arms and with 40-km arms), and, by comparison, with the ASD expected for LIGO and Virgo by the end of the O5 run.¹

The question that we want to address in this paper is what happens when one combines a single L-shaped detector with the ASD of ET (therefore underground, and made of a LF and a HF interferometer), with a single 3G L-shaped detector on the surface, again located in Europe. For instance, a very interesting question is whether the better low-frequency sensitivity of a single L-shaped detector with the ASD of ET becomes of limited value, without a partner with a similar low-frequency sensitivity or, on the contrary, it is sufficient to combine it with a 3G surface detector to exploit its low-frequency capabilities. For the underground L-shaped detector we will use the most recent publicly available ET curve (shown in Figure 1). This is the same sensitivity curve that was also used in the study [17]. For the surface L-shaped European detector we will use, as an example, the ASD of a 20-km CE detector. On the basis of the analysis made during the ET conceptual design, one should not expect that the CE sensitivity can be easily realized with a surface detector in Europe due to strong constraints on interferometer length. We use it in our analysis since it is the only readily available model of a sensitivity curve for a next-generation GW detector at the surface.²

¹When comparing a triangle to an L-shaped interferometer with the same ASD, one must take into account that the triangle is made of three nested detectors (a detector being an LF and HF interferometer pair), with an opening angle of 60° . For the triangle configuration, one must then project the GW tensor of the incoming wave onto each of these three components [see eqs. (9)–(11) of [23] for explicit expressions], and then combine the results at the level of the SNR and parameter estimation to obtain the ET capabilities. See also the discussion in Section 2 of ref. [17].

²The ET sensitivity curve that we use is available at <https://apps.et-gw.eu/tds/?content=3&r=18213>. For CE–20km and CE–40km we use the curves available at <https://dcc.cosmicexplorer.org/cgi-bin/DocDB/ShowDocument?.submit=Identifier&docid=T2000017&version=>. Again, these are the same sensitivity curves that have been used in ref. [17].

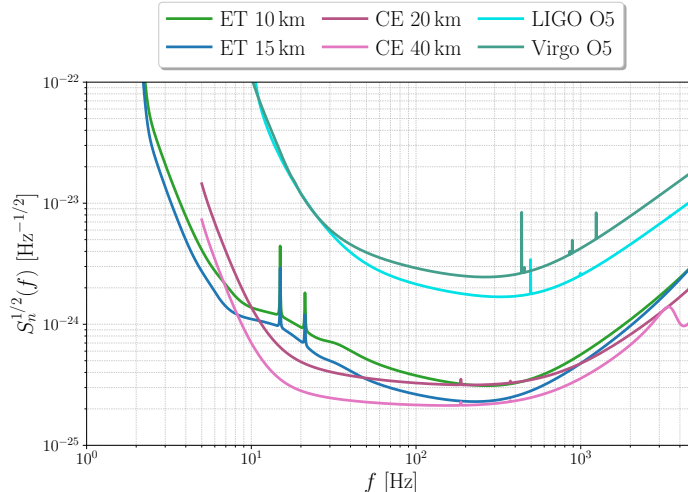


Figure 1. Amplitude spectral densities (ASDs) used in this work. Note that the ASDs are always defined as if we had a single L-shaped detector of the given arm-length. To get the overall sensitivity of the triangle to a given signal, one must then combine the ASD of the three interferometers as discussed in [footnote 1](#).

More in detail, we consider the following configurations:

- ET in its standard 10-km triangle configuration. We will refer it as ET- Δ .
- ET in the configuration of two L-shaped detectors with 15 km arms, taken to be in the two candidate sites in Sardinia and in the Meuse-Rhine region. We will refer to it as ET-2L (see below for the relative orientation among the two L).
- A hybrid configuration of two detectors, both taken to be in Europe, one L-shaped, underground and with the ASD of ET with 15 km arms, and the other again L-shaped but on the surface, with the ASD of CE, with 20 km arms. We will refer to it as “Hybrid”.

Each of these configurations will then be studied also in correlation with a single 40-km CE located in the US.

The first two configurations above are the two main reference configurations that were studied in [\[17\]](#), and they are both being actively considered for ET.³ The Hybrid configuration, in contrast, has never been considered to date. Placing a 20-km interferometer on the surface, as in the Hybrid configuration, requires a sufficiently large underpopulated area, both to construct such a long infrastructure and to avoid anthropic noise. In Europe it is

³Their different arm-lengths reflect the fact that the total length of the vacuum pipes to be installed (which is one of the most expensive items) is the same for a 10-km triangle and for a 15-km 2L. Indeed, for the triangle we have 3 tunnels and 4 vacuum tubes per tunnel (since, in a nested detector configuration, in each tunnel we have one arm of the HF interferometer and one arm of the LF interferometer of one detector, as well as one arm of the HF interferometer and one arm of the LF interferometer of another detector), so $10 \text{ km} \times 3 \times 4 = 120 \text{ km}$, while for 2L we have overall 4 arms, but just 2 tubes per arm (the HF and the LF interferometers), and $15 \text{ km} \times 4 \times 2 = 120 \text{ km}$ [\[24\]](#). Furthermore, taking into account that the nested detectors configuration of the triangle requires larger tunnels, also the volume of excavated rocks (another crucial aspects of a cost analysis) for a 10-km triangle and for a 15-km 2L is roughly comparable, see also footnote 5 in [\[17\]](#).

more difficult to find viable sites of this type, compared to the US. Here, for the sake of the exercise, we will put the single-L surface detector in a largely underpopulated area in Spain⁴ and, for definiteness, in the Hybrid configuration we will locate the single-L detector with the ET ASD in the Sardinia candidate site, resulting in a cord-distance of about 1300 km. Similar results would, however, be obtained placing the surface detector elsewhere in Spain, or in fact in any suitable place in Europe, as well as placing the underground detector in any of the two candidate locations in Europe, as long as the two sites have a similar cord distance; in particular, this holds for a surface detector in this hypothetical site in Spain and an underground detector in the Meuse-Rhine candidate site, as the cord distance in this case is about 1390 km. We stress that the specific choice that we make here for the location of a surface detector as well as, more generally, the choice of studying a configuration of a single L-shaped ET-like underground detector, and a single L-shaped 3G on-surface detector, both located in Europe, does not correspond to any project currently under study from the many points of view (geological, topographical, financial, political, etc.) that are necessary for determining viable detector configurations and optimal site selection. At the present stage, this must just be considered as an exercise, whose aim is to better understand the performances of 3G networks in different settings.

In a 2L network an important choice is the relative orientation among the two detectors. When taking into account the Earth’s curvature, the relative orientation between two L-shaped detectors is defined with reference to the great circle that connects them [25, 26]. We denote by β the angle describing the relative orientation of the two detectors, defined with reference to this great circle, so that $\beta = 0^\circ$ corresponds to the case where the arms of the two interferometers make the same angle with respect to the great circle, while $\beta = 45^\circ$ corresponds to the situation in which one of the two interferometers is rotated by 45° from the $\beta = 0^\circ$ orientation. For $\beta = 45^\circ$ the accuracy of the parameter estimation for coalescing binaries is maximized,⁵ while the sensitivity to stochastic backgrounds is minimized (to the extent that it becomes exactly zero in the limit $d/\lambda \rightarrow 0$, where $\lambda = c/f$ is the wavelength of a GW with frequency f , and d the distance between the two detectors). Conversely, for parallel detectors ($\beta = 0^\circ$) the sensitivity to stochastic background is maximized, while the accuracy of the parameter estimation for coalescing binaries is minimized.⁶ Here we will follow the same strategy as in ref. [17], considering both the case $\beta = 0^\circ$, and the case of β close, but not exactly equal, to 45° , using a value $\beta = 45^\circ - 2.51^\circ$. This small misalignment, with respect to $\beta = 45^\circ$, has essentially no impact on the quality of the reconstruction of the parameters of coalescing binaries, while it allows us to recover an interesting sensitivity to stochastic backgrounds, about 10% of the optimal sensitivity which is obtained for parallel detectors.⁷ We will denote the corresponding 2L configurations as 2L- 0° (i.e. $\beta = 0^\circ$) and

⁴We use for definiteness the coordinates ($41^\circ 21' 57''$ N, $6^\circ 06' 4''$ O), that fall inside a large flat and desert area with a population density of 6 persons/km², with the closest town having about 1000 inhabitants.

⁵Actually, this is true only for the standard tensorial polarization of General Relativity (GR), and not for extra polarization modes that could appear in extensions of GR.

⁶Note, however, that for parallel detectors the sensitivity to parameter estimation is of course non-zero and in fact still reasonably close to the optimal value. The two LIGO detectors are set parallel to each other, as was natural for two detectors whose initial target was to get the first detections, in which case one maximizes the chances that the two detectors both go above detection threshold for the same event.

⁷The precise value 2.51° of the misalignment angle has no special meaning. It was chosen, somewhat arbitrarily, in ref. [17] because, for the case of one detector in the Sardinia candidate site and one in the Meuse-Rhine candidate site, it corresponds to $\alpha = 45^\circ$, where α is the relative angle defined using the local North at the two detector sites; i.e., for these specific locations, $\alpha \simeq \beta + 2.51^\circ$.

2L-mis (for misaligned, i.e. $\beta = 45^\circ - 2.51^\circ$).⁸ So, more precisely, the all-European networks that we will consider are:

1. ET- Δ : the 10-km triangle, with the ET ASD, therefore underground. We locate it for definiteness in Sardinia.
2. ET-2L- 0° : two L-shaped detectors of 15 km arms, with the ET ASD, therefore both underground, taken to be parallel with respect to the great circle that joins them (i.e. $\beta = 0^\circ$). We locate them in Sardinia and in the Meuse-Rhine region.
3. ET-2L-mis: as ET-2L- 0° , but at $\beta = 45^\circ - 2.51^\circ$.
4. Hybrid- 0° : a hybrid configuration, with an underground L-shaped detector with the ASD of ET with 15 km arms (located for definiteness in Sardinia) and a surface L-shaped detector with the ASD of CE-20km (located as an example in Spain, with a baseline among the two sites of order 1300 km).
5. Hybrid-mis. As Hybrid- 0° , but at $\beta = 45^\circ - 2.51^\circ$.

We will also compare with the results that could be obtained by the most advanced 2G detector network, namely LIGO Hanford, LIGO Livingston, Virgo, KAGRA and LIGO India, using the publicly available best sensitivities that are planned to be achieved by the end of the O5 run [27]. We denote this network as LVKI O5.

Finally, each of the five European networks above will also be studied in a broader world-wide network, adding further a single-L CE detector of 40 km in the US.⁹ We observe that the recent report of the NSF MPS AC Subcommittee on Next-Generation Gravitational-Wave Detector Concepts [15] includes a network of CE-40km and ET (taken in its ET- Δ configuration) among the recommended world-wide next-generation networks. Our analysis will allow us to compare also with different possible versions of a European project, such as the ET-2L, or the Hybrid configurations.

3 Methodology

Our methodology is identical to the one already followed in Section 3 of ref. [17], whom we refer the reader for more details. For compact binary coalescences (CBCs), we perform parameter estimation in the Fisher matrix approximation, using the **GWFAST** code [29, 30].¹⁰ **GWFAST** is a Fisher matrix code tuned toward the needs of 3G detectors. In the context of the activities of the ET Observational Science Board (OSB),¹¹ extended cross-checks

⁸Actually, the only situation for which the precise value 2.51° of the misalignment angle is relevant is for the study of stochastic backgrounds in the misaligned configuration. For all results on compact binary coalescences, the plots of the results obtained with $\beta = 45^\circ - 2.51^\circ$, on the scales that we use, are visually indistinguishable from those with $\beta = 45^\circ$; similarly for $\beta = 0^\circ$ or $\beta = -2.51^\circ$.

⁹When performing the correlation with a 40-km CE in the US, we will place for definiteness the US detector in Idaho using as representative the location and orientation in Table III of [28]. This results in an alignment of about 191° with respect to the Sardinia site, 237° with respect to the Meuse-Rhine site (in the situation in which this is misaligned with respect to the Sardinia one) and 227° with respect to the Spain site (in the situation in which this is misaligned with respect to the Sardinia one). We stress that the exact choice for the location is not relevant as far as it can provide a long baseline when in a network with European detectors.

¹⁰The code is publicly available at <https://github.com/CosmoStatGW/gwfast>.

¹¹See <https://www.et-gw.eu/index.php/the-et-collaboration/observational-science-board>.

have performed between GWFAST and other recently developed Fisher-matrix codes for 3G detectors, such as GWBENCH [28], GWFISH [31], TiDoFM [32, 33] and the code used in [34]. The Fisher matrix formalism has well-known limitations [35, 36], but is currently the only computationally practical way of dealing with parameter estimation for large populations (see, however, ref. [37] for progress toward the use of full inference on large populations, and ref. [38] for a mixed approach in which some parameters are dealt analytically while some are dealt with the Fisher matrix).

We use state-of-the-art waveforms; for binary black holes (BBHs) we use IMRPHENOMXPHM (which includes precessing spins and higher-order modes) [39]. For binary neutron stars (BNSs) we use IMRPHENOMD_NRTIDALV2 [40, 41], which includes tidal effects. The parameters of the waveform are

$$\{\mathcal{M}_c, \eta, d_L, \theta, \phi, \iota, \psi, t_c, \Phi_c, \chi_1, \chi_2, \Lambda_1, \Lambda_2\}, \quad (3.1)$$

where \mathcal{M}_c is the detector-frame chirp mass, η the symmetric mass ratio, d_L the luminosity distance to the source, θ and ϕ the sky position coordinates, ι the angle between the orbital angular momentum of the binary and the line of sight, ψ the polarisation angle, t_c the time of coalescence, Φ_c the phase at coalescence, χ_i the dimensionless spin vector of the component $i = \{1, 2\}$ of the binary, and Λ_i their dimensionless tidal deformabilities. Instead of Λ_1, Λ_2 , we will actually use the two combinations $\tilde{\Lambda}$ and $\delta\tilde{\Lambda}$ defined in [42]. We will show the results for the combination

$$\tilde{\Lambda} = \frac{8}{13} \left[(1 + 7\eta - 31\eta^2)(\Lambda_1 + \Lambda_2) + \sqrt{1 - 4\eta}(1 + 9\eta - 11\eta^2)(\Lambda_1 - \Lambda_2) \right], \quad (3.2)$$

which enters at 5PN order, while $\delta\tilde{\Lambda}$ only enters at 6PN and is more poorly constrained. For BBHs we will perform the inference on all parameters except, of course, the tidal deformabilities, that vanish for BHs and, as in LVK parameter estimations, rather than ι , we will use θ_{JN} , defined as the angle between the total angular momentum and the line of sight; this is the same as ι only in the absence of precession. For BNSs, instead, we include tidal deformability but, given the small expected values of their spin magnitudes, we only consider the aligned spin components in the analysis, thus performing estimation on $\chi_{1,z}$ and $\chi_{2,z}$. The labels ‘1’ and ‘2’ always refer, respectively, to the heaviest and lightest component of the binary system.

We also use state-of-the-art population models; in particular, we use the same catalog of BBH and BNS already used in [17].¹² The catalog for BNSs is based on work developed in refs. [43–48], while the catalog of BBHs is based on [49, 50].

As in [17], we assume an uncorrelated 85% duty cycle in each L-shaped detector, and in each of the three detectors composing the triangle. All other technical details of the inference process performed below are as described in [17, 29].

4 Results

4.1 Horizons

Figure 2 shows the detector horizons for the detector networks considered, as a function of the total mass of the binary, for equal-mass non-spinning coalescing binaries. The left panel gives the results for the 3G European networks that we are considering (and, for comparison,

¹²These catalogs are publicly available at <https://apps.et-gw.eu/tds/?content=3&r=18321>.

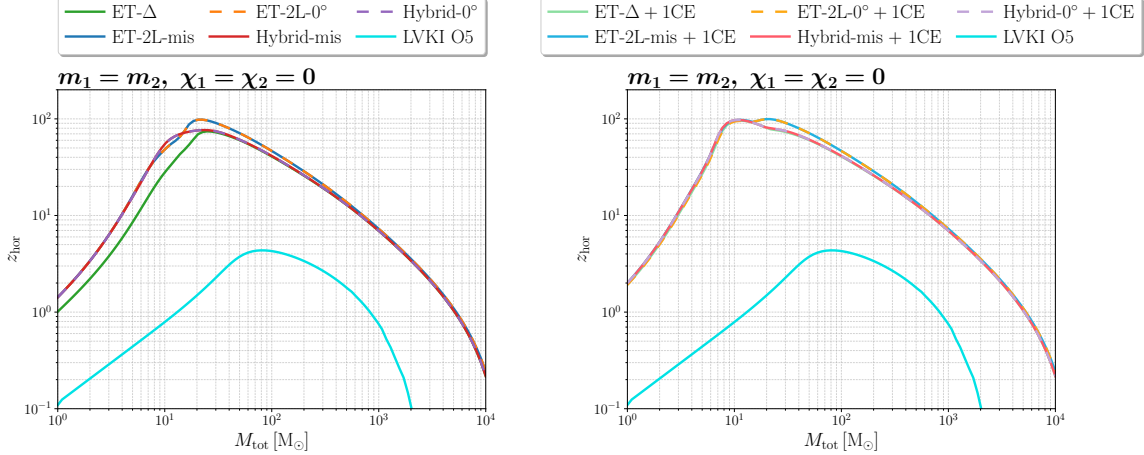


Figure 2. Detector horizons for equal mass, non-spinning binaries for the various detector geometries considered for European-only networks (*left panel*), and adding to each 3G network a single 40-km CE detector in the US (*right panel*). In each panel we also add, for comparison, LVKI O5. On the scale of the figure, ET-2L-0° and ET-2L-mis are indistinguishable, and the same for Hybrid-0° and Hybrid-mis.

also LVKI O5), while in the right panel each of these 3G European-only networks is further enlarged by adding a 40-km CE located in the US (and we compare again also LVKI O5). Note that, on this logarithmic scale, the difference between the 2L configurations misaligned or at 0° are not visible.

First of all, [Figure 2](#) shows that, in terms of detection horizons, each of these 3G configurations allows us to make a large jump with respect to the best possible 2G detector network. We also see that, above a few hundreds M_{\odot} , all the 3G networks in the left panel have very similar detection horizons; below about 20 M_{\odot} , however, in the European-only setting some difference appear, and the ET- Δ configuration is less performant, while the ET-2L and Hybrid configurations have rather similar horizons. In particular, for $M_{\text{tot}} = 2.7 M_{\odot}$, a typical value for the total mass of a BNS, the values of the horizons for the 3G configurations in the left panel are given in [Table 1](#), where we see that, for BNS, all networks reach $z_{\text{hor}} \simeq 5.3$ except ET- Δ , that reaches $z_{\text{hor}} \simeq 3.3$. In contrast, we see from the right-panel of [Figure 2](#) that, when CE-40km is added, the redshift horizons become closer to each other, almost everywhere in the mass range shown. For $M_{\text{tot}} = 2.7 M_{\odot}$, the horizons are given in the right panel of [Table 1](#), and they are all between 8.4 and 9.0. Note that, in any case, all these configurations cover the peak of the star formation rate, at $z \sim 2 - 3$, and therefore the large majority of BNSs.

The detection of subsolar-mass black holes would be a smoking gun signature for their primordial origin. For an equal-mass binary with total mass $M_{\text{tot}} = 1.0 M_{\odot}$ (i.e., a $0.5 M_{\odot} + 0.5 M_{\odot}$ binary), the horizon of all European configurations is $z_{\text{hor}} \simeq 1.4$, except for ET- Δ , for which $z_{\text{hor}} \simeq 1.0$. Once put into a network with the 40-km CE in the US, however, all these configuration have z_{hor} between 1.9 and 2.0.

Of course, the detection horizons only tell us a part of the story, and the accuracy of parameter estimation depends significantly also on other aspects (see e.g. [\[29, 51–56\]](#) for discussions in the context of 3G detectors). As an example, the angular resolution of a network of two L-shaped interferometers is very sensitive to the relative orientation between

Detector configuration	$z_{\text{hor}}(2.7 M_{\odot})$	Detector configuration	$z_{\text{hor}}(2.7 M_{\odot})$
ET- Δ	3.3	ET- Δ + 1CE	8.5
ET-2L-mis	5.3	ET-2L-mis + 1CE	9.0
ET-2L-0 $^{\circ}$	5.3	ET-2L-0 $^{\circ}$ + 1CE	8.4
Hybrid-mis	5.3	Hybrid-mis + 1CE	8.9
Hybrid-0 $^{\circ}$	5.3	Hybrid-0 $^{\circ}$ + 1CE	8.9
LVKI O5	0.3	LVKI O5	0.3

Table 1. Horizon redshifts for equal mass non-spinning binaries evaluated at a source-frame total mass $M_{\text{tot}} = 2.7 M_{\odot}$ for the various configurations considered without (*left table*) and with (*right table*) a single 40-km CE detector in the US.

the two Ls, and to the distance between the detectors. In the next subsection we then examine the performances of these configurations for parameter estimation of coalescing binaries.

4.2 Parameter reconstruction of coalescing binaries

4.2.1 European networks

We begin by considering the networks where all 3G detectors are located in Europe. [Figure 3](#) shows the cumulative distributions of the number of detections per year, for the network SNRs and for the error on the parameters, for BBH signals. We see that the most significant differences appear in the SNR distribution, angular localization, and luminosity distance. For the SNR distributions, among the 3G networks, the ET- Δ configuration is noticeably less performant, even on this logarithmic scale, while all others 3G configurations are equivalent. For angular resolution, the best results come from ET-2L-mis and Hybrid-mis, which are very similar among them, and clearly better than ET- Δ , which in turn is clearly better than ET-2L-0 $^{\circ}$ and Hybrid-0 $^{\circ}$. For the accuracy on the luminosity distance, again ET-2L-mis and Hybrid-mis are very similar among them and provide the best results, followed in this case by ET-2L-0 $^{\circ}$ and Hybrid-0 $^{\circ}$, while ET- Δ is the less performing configuration. Note that, for angular localization, LVKI at O5 sensitivity is very competitive, given that it is composed by five detectors, with large baselines among them; indeed, for events localized better than a few degrees, only ET-2L-mis and Hybrid-mis perform better than LVKI O5. [Table 2](#) gives, for each of these 3G networks, the number of BBHs with angular resolution $\Delta\Omega_{90\%}$ (defined, as in [\[17\]](#), as the sky localisation area at 90% c.l.) smaller than 1 deg^2 , or smaller than 10 deg^2 (first two column), as well as the BBHs that (independently of their angular localization) have $\Delta d_L/d_L \leq 5 \times 10^{-3}$, or $\Delta d_L/d_L \leq 10^{-2}$ (third and fourth column).¹³ Observe, in particular, that for BBHs with d_L measured better than 1%, we have 217 events for Hybrid-mis and 28 for ET- Δ , a difference by one order of magnitude. For all other parameters the differences are not so significant (except, more marginally, for θ_{JN}).

[Figure 4](#) shows the distribution in redshift of “golden events” defined, as in ref. [\[17\]](#), as events with especially high SNR (left column), or especially good reconstruction of luminosity distance (middle column) or of sky location (right column), for BBHs in these European-only networks. We observe that, also on this metric, ET-2L-mis and Hybrid-mis give the best performance in all three panels; in the case of the SNR, also ET-2L-0 $^{\circ}$ and Hybrid-0 $^{\circ}$ perform very well; however, the -0 $^{\circ}$ configurations are again the less performant, among the

¹³All these figures are for one year of data taking, with the duty cycles given at the end of [Section 3](#).

BBH

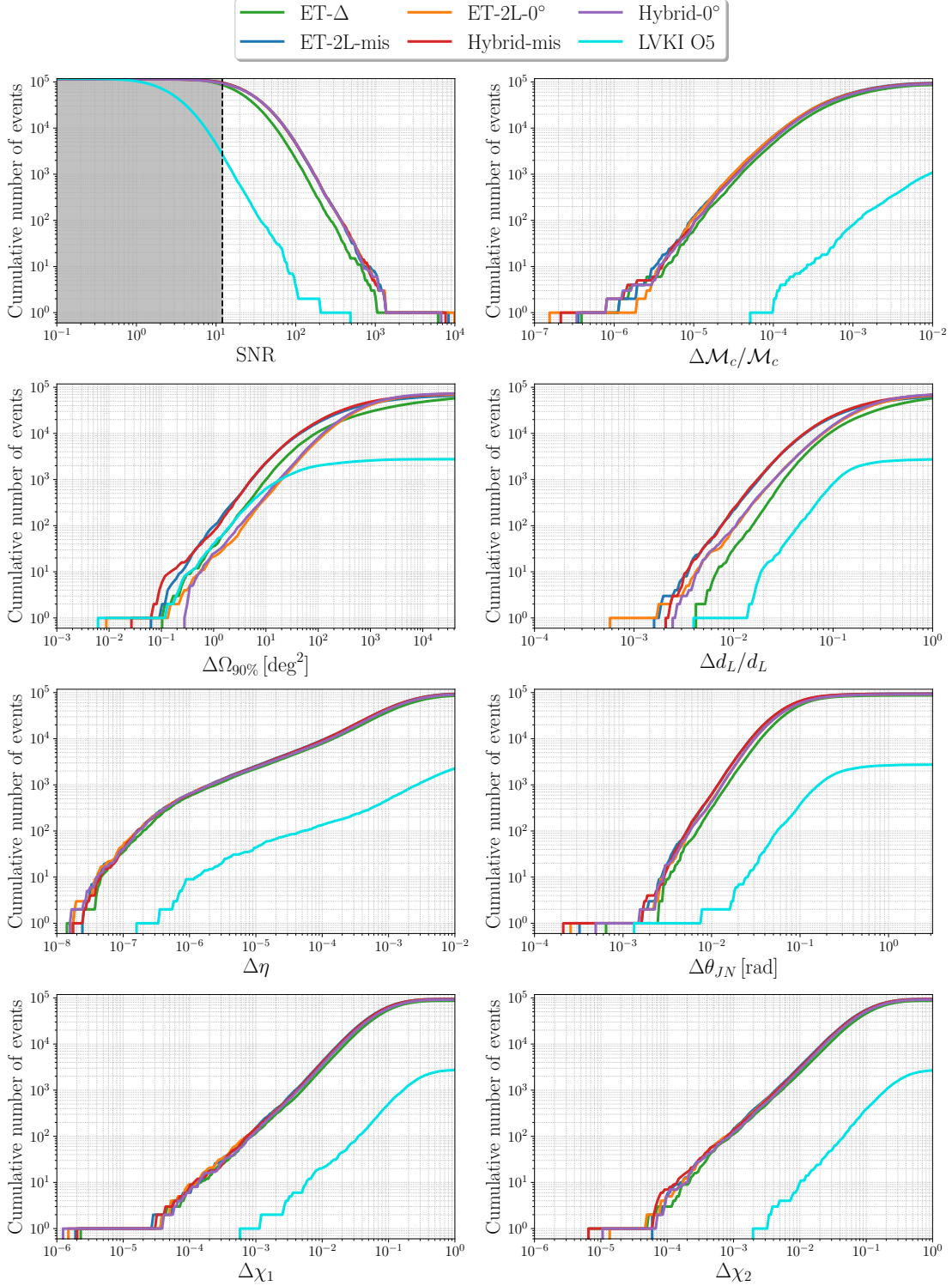


Figure 3. Cumulative distributions of the number of detections per year, for the SNRs and for the error on the parameters, for BBH signals, for the European networks considered.

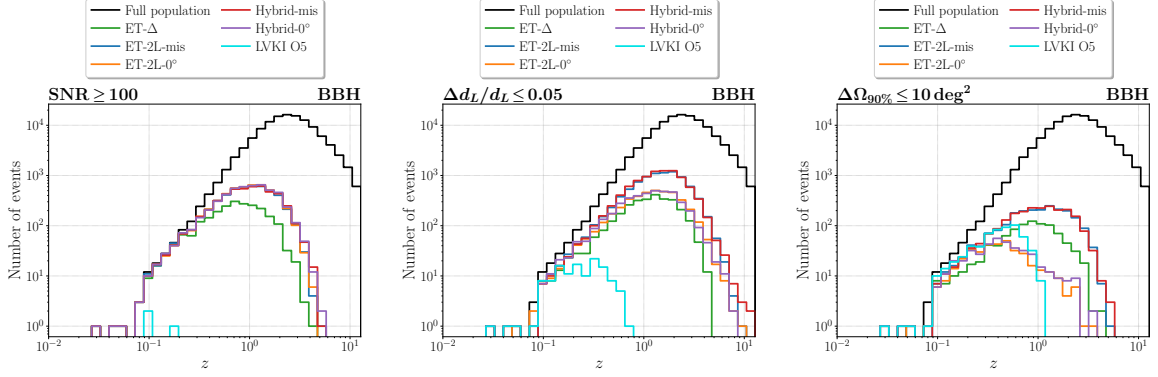


Figure 4. Redshift distribution of BBHs detected with $\text{SNR} \geq 100$ (left column), relative error on the luminosity distance $\Delta d_L/d_L \leq 0.05$ (central column), or sky location $\Delta\Omega_{90\%} \leq 10 \text{ deg}^2$ (right column) for the various detector geometries considered with all detectors located in Europe.

3G configurations, for events with especially good angular localizations. Note, however, that all 3G configurations now perform much better than LVKI O5 for well-localized events at large redshift. LVKI O5 has no BBH localized to better than 10 deg^2 beyond $z = 1$, while all other 3G networks detect hundreds of events with this localization at $z > 1$, and a few of them even up to $z \sim 3 - 4$.

BBH				
Detector configuration	Detections with			
	$\Delta\Omega_{90\%} \leq$		$\Delta d_L/d_L \leq$	
	1 deg ²	10 deg ²	5×10^{-3}	10^{-2}
ET-Δ	35	914	2	28
ET-2L-mis	92	2 124	29	202
ET-2L-0°	21	374	15	79
Hybrid-mis	70	2 180	32	217
Hybrid-0°	24	416	17	84

Table 2. Number of detected BBH sources at the considered European networks with different cuts on the sky localization or on the relative error on the luminosity distance.

Figures 5 and 6 show the corresponding results for BNS. From Figure 5 we see that, for angular localization, ET-2L-mis is better than the other configurations, which are close among them, especially for localizations better than 100 deg^2 . For luminosity distance, ET-2L-mis is clear the best, followed by Hybrid-mis, which in turn is clearly better than ET-Δ and ET-2L-0°. Table 3 gives, for each of these networks, the number of BNSs with $\Delta\Omega_{90\%} \leq 10 \text{ deg}^2$ or with $\Delta\Omega_{90\%} \leq 100 \text{ deg}^2$, and the number of BNSs that (independently of their angular localization) have $\Delta d_L/d_L \leq 5 \times 10^{-2}$, or $\Delta d_L/d_L \leq 10^{-1}$.

Observe that the Hybrid-mis configuration actually localizes BNS somewhat better than ET-Δ: for $\Delta\Omega_{90\%} \leq 10 \text{ deg}^2$ it has 12 events against 8, while for $\Delta\Omega_{90\%} \leq 100 \text{ deg}^2$ it has 288 events against 184. It is instructive to understand the mechanism behind this result. In general, a better low-frequency sensitivity allows BNSs to stay longer in the bandwidth, up to

several hours or a day; then, the modulation of the signal due to Earth’s rotation (which is an effect taken into account in **GWFAST**) allows us to improve the angular localization; since ET- Δ has a better low-frequency sensitivity than Hybrid-mis, this effect favors ET- Δ over Hybrid-mis. On the other hand, two well-separated detectors can better triangulate the signal, with respect to a single-site detector, and this favors Hybrid-mis over ET- Δ . We see that, overall, in the comparison among these two configurations, the effect of the long baseline dominates. On the other hand, ET-2L-mis benefits of both effects (better low-frequency sensitivity and long baseline) and has clearly the best performances, with 25 BNS localized better than 10 deg^2 , and 559 better than 100 deg^2 .

From [Figure 5](#) we see that significant differences also show up in the polarization angle ψ and in orbit inclination θ_{JN} , where the parallel configurations (and, for ψ , ET- Δ), clearly perform less well. In general, whatever the observable, we always find that, among the 3G networks, ET-2L-mis and Hybrid-mis are the two top performers, sometime with clear differences with respect to the other configurations, sometime together with other configurations. The same message emerges from the golden BNS events in [Figure 6](#). Note, however, that the LVKI-O5 network, while clearly inferior for all other observables, is the one that get the best results for events with angular localization below a few degrees, thanks to the fact of being made by five detectors, with large baseline distances.

BNS

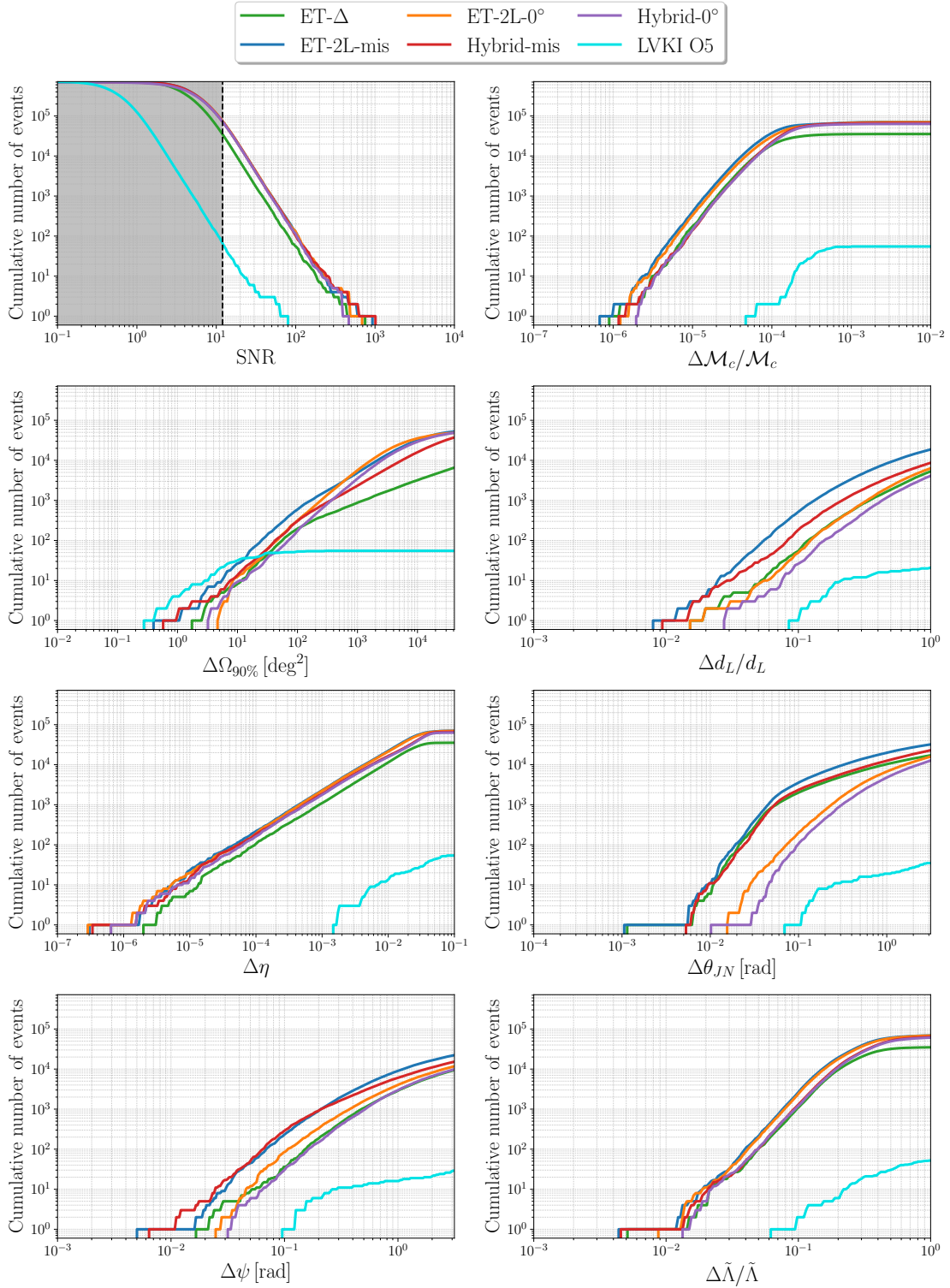


Figure 5. Cumulative distributions of the number of detections per year, for the SNRs and for the error on the parameters, for BNS signals, for the European networks considered.

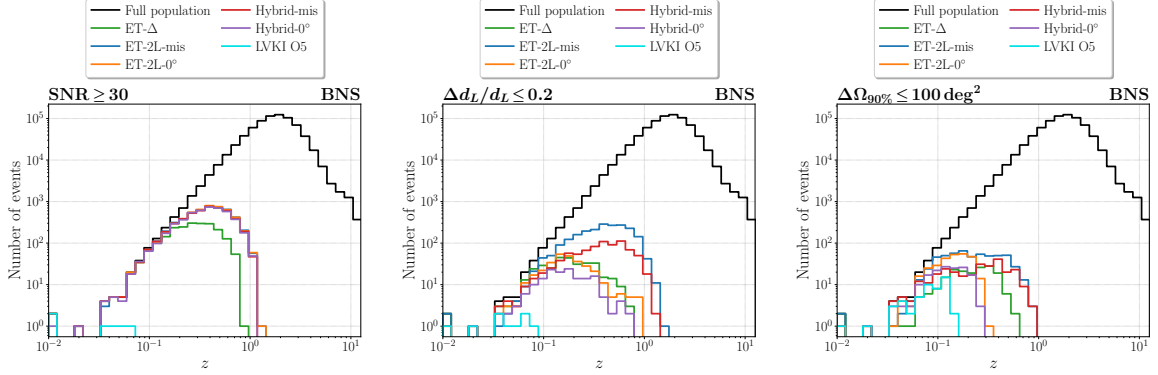


Figure 6. Redshift distribution of BNSs detected with $\text{SNR} \geq 30$ (left column), relative error on the luminosity distance $\Delta d_L/d_L \leq 0.2$ (central column), or sky location $\Delta\Omega_{90\%} \leq 100 \text{ deg}^2$ (right column) for the various detector geometries considered with all detectors located in Europe.

BNS				
Detector configuration	Detections with			
	$\Delta\Omega_{90\%} \leq$		$\Delta d_L/d_L \leq$	
	10 deg^2	100 deg^2	5×10^{-2}	10^{-1}
ET- Δ	8	184	8	52
ET-2L-mis	25	559	69	479
ET-2L- 0°	12	293	7	48
Hybrid-mis	12	288	28	169
Hybrid- 0°	9	157	4	25

Table 3. Number of detected BNS sources at the considered European networks with different cuts on the sky localization and relative error on the luminosity distance.

4.2.2 European networks together with a CE-40km in the US

We now consider a set of broader world-wide networks, in which we add a 40-km CE detector in the US to each of the 3G European configurations studied in the previous subsection. The results are given in [Figures 7 and 8](#) for BBHs, and in [Figures 9 and 10](#) for BNSs.

We see that, for BBHs, all network configurations become essentially equivalent, on all observables.¹⁴ This is confirmed by the values given in [Table 4](#).

For BNSs the differences are larger, in particular for angular localization and luminosity distance, where the best results are obtained by (ET-2L-mis + 1CE) and (Hybrid-mis + 1CE), that are typically better by a factor of order 2 than ET- Δ , which in turn is somewhat better than (ET-2L- 0° + 1CE) and (Hybrid- 0° + 1CE). As an example, [Table 5](#) gives, for each of these networks, the number of BNSs with $\Delta\Omega_{90\%} \leq 10 \text{ deg}^2$ or with $\Delta\Omega_{90\%} \leq 100 \text{ deg}^2$, as well as the BNSs that (independently of their angular localization) have $\Delta d_L/d_L \leq 5 \times 10^{-2}$, or $\Delta d_L/d_L \leq 10^{-1}$ (again, for one yr of data and our choice of duty cycle).

¹⁴The results for ET- Δ , ET-2L-mis and ET-2L- 0° , together with 1CE, are the same already shown in [Figure 18](#) of [\[17\]](#). In that figure, the spread in the results looked visually larger because, there, were included also the configurations with 2 CE in the US.

BBH

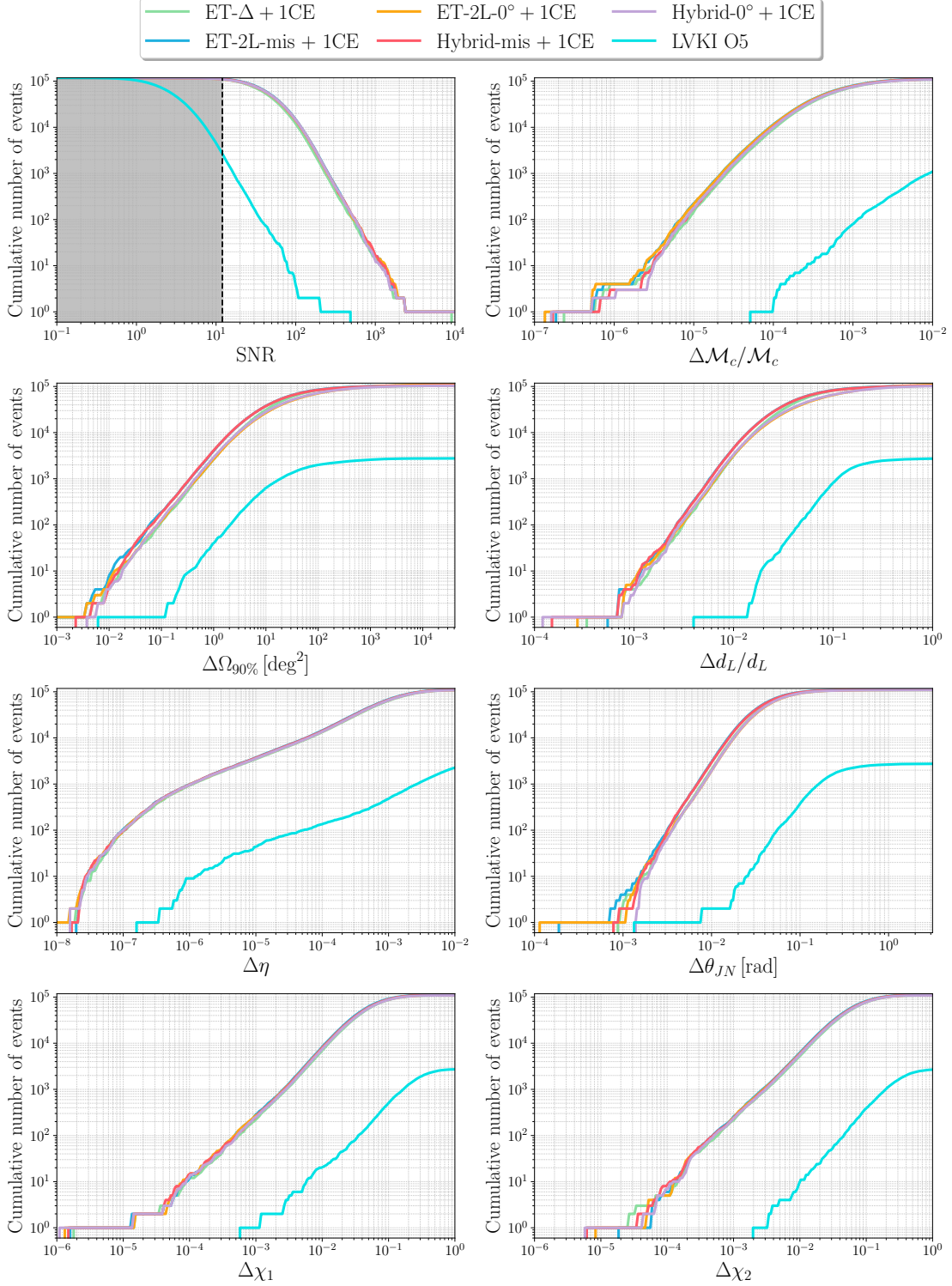


Figure 7. Cumulative distributions of the number of detections per year, for the SNRs and for the error on the parameters, for BBH signals, for the various detector geometries considered, including a single 40-km CE detector in the US.

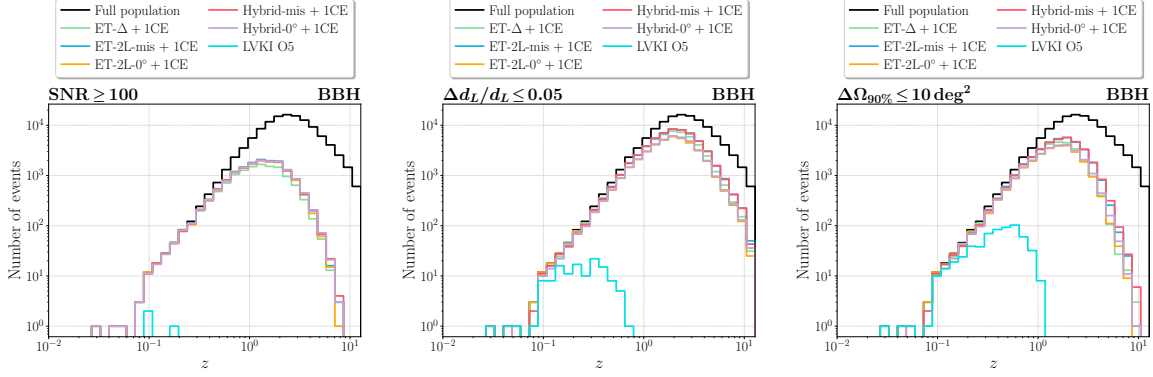


Figure 8. Redshift distribution of BBHs detected with $\text{SNR} \geq 100$ (left column), relative error on the luminosity distance $\Delta d_L/d_L \leq 0.05$ (central column), or sky location $\Delta\Omega_{90\%} \leq 10 \text{ deg}^2$ (right column) for the various detector geometries considered, including a single 40-km CE detector in the US.

BBH				
Detector configuration	Detections with			
	$\Delta\Omega_{90\%} \leq$		$\Delta d_L/d_L \leq$	
	1 deg ²	10 deg ²	5×10^{-3}	10^{-2}
ET- Δ + 1CE	2 447	29 924	395	2 901
ET-2L-mis + 1CE	3 743	36 457	575	4 301
ET-2L-0° + 1CE	2 464	25 782	400	2 995
Hybrid-mis + 1CE	3 810	36 344	581	4 276
Hybrid-0° + 1CE	2 704	27 043	433	3 153

Table 4. Number of detected BBH sources at the considered networks including a single 40-km CE detector in the US, with different cuts on the sky localization and relative error on the luminosity distance.

Significant differences appear also for the polarization angle and the orbit inclination, for which again (ET-2L-mis + 1CE) and (Hybrid-mis + 1CE) are the best configurations.

BNS

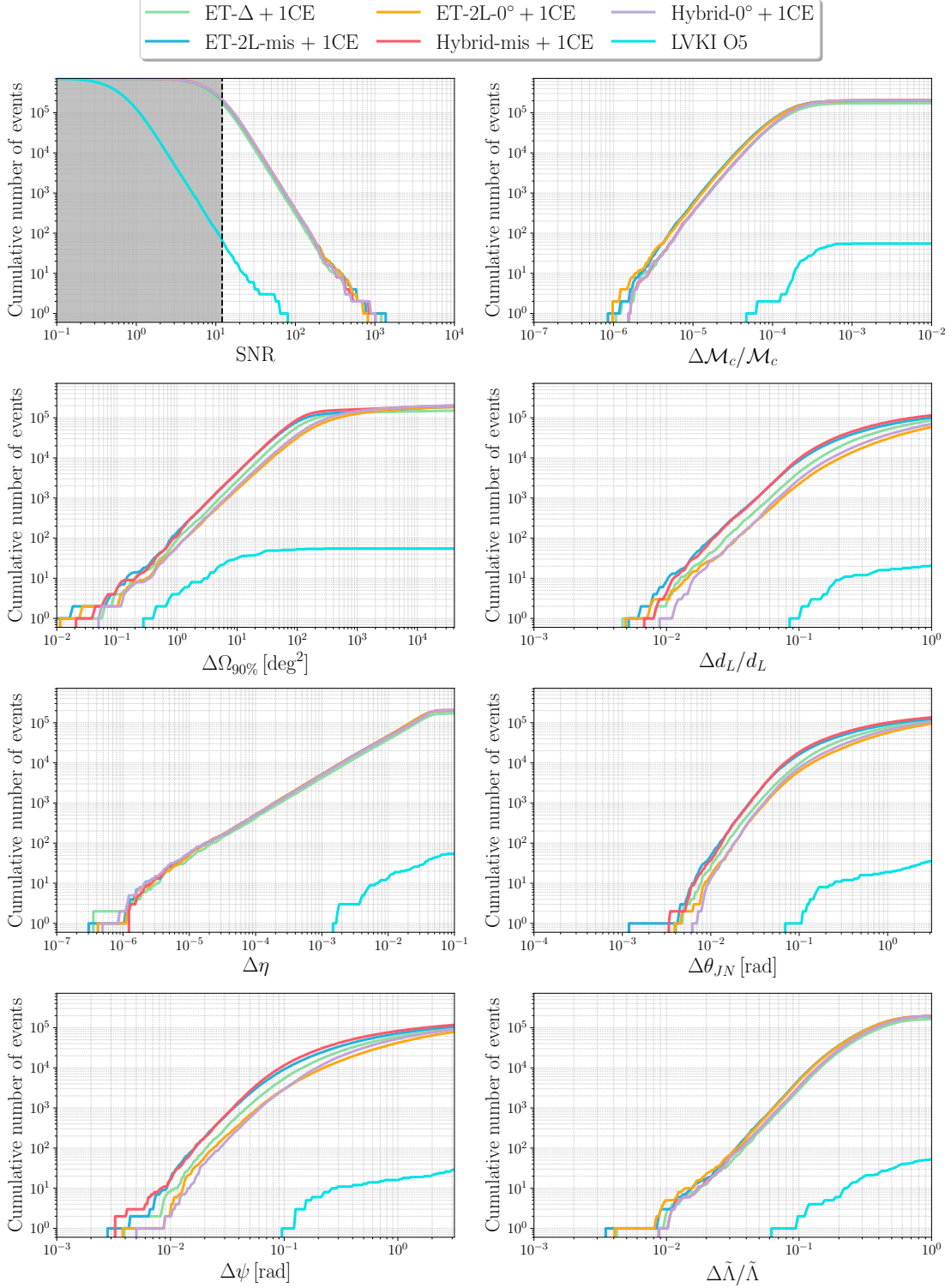


Figure 9. Cumulative distributions of the number of detections per year, for the SNRs and for the error on the parameters, for BNS signals, for the various detector geometries considered, including a single 40-km CE detector in the US.

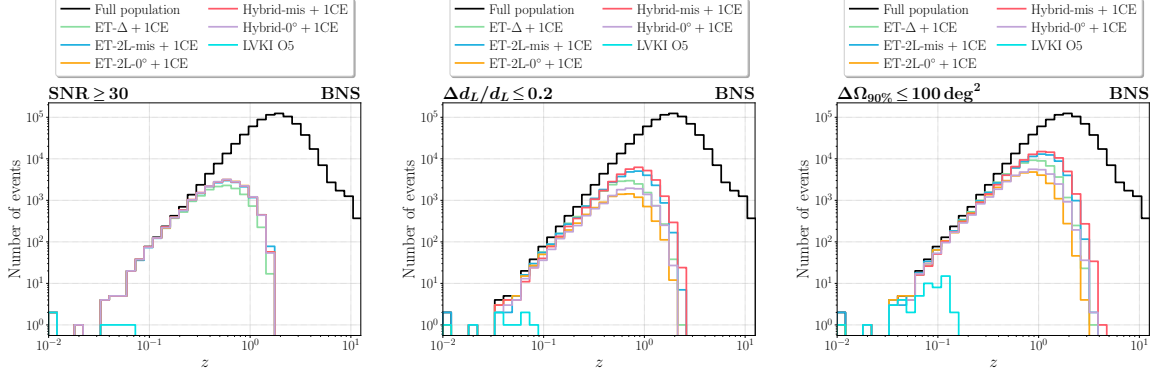


Figure 10. Redshift distribution of BNSs detected with $\text{SNR} \geq 30$ (left column), relative error on the luminosity distance $\Delta d_L/d_L \leq 0.2$ (central column), or sky location $\Delta\Omega_{90\%} \leq 100 \text{ deg}^2$ (right column) for the various detector geometries considered, including a single 40-km CE detector in the US.

BNS				
Detector configuration	Detections with			
	$\Delta\Omega_{90\%} \leq$		$\Delta d_L/d_L \leq$	
	10 deg^2	100 deg^2	5×10^{-2}	10^{-1}
ET- Δ + 1CE	2 427	54 994	535	4 100
ET-2L-mis + 1CE	3 838	75 828	1 040	7 949
ET-2L- 0° + 1CE	1 515	29 821	288	2 079
Hybrid-mis + 1CE	3 932	85 140	1 043	8 961
Hybrid- 0° + 1CE	1 704	35 608	294	2 710

Table 5. Number of detected BNS sources at the considered networks including a single 40-km CE detector in the US, with different cuts on the sky localization and relative error on the luminosity distance.

4.3 Pre-merger alerts

The low-frequency sensitivity is particularly important for detecting inspiralling binaries early enough, so to be able to send alerts to electromagnetic observatories. From this point of view, two aspects are important. One is how the SNR accumulates in the different detector networks, allowing for an early detection.¹⁵ The second is how well one can give the angular localization to electromagnetic observatories, sufficiently early before the merger takes place.

Figure 11 shows how the SNR would accumulate in the various 3G networks considered, for an event with the characteristics of GW170817, as the signal sweeps up in frequency. The left panel shows the result for the European networks, while the right panel gives the result when the 40-km CE in the US is added. The lower horizontal axis gives the frequency of the signal, while the upper horizontal axis gives the corresponding time to merger. For this event, which was so close in distance, all network configurations considered reach very rapidly a large SNR. A SNR larger than a detection threshold, say set at $\text{SNR} = 12$, is reached in all case about 10 hours prior to merger, and 20 minutes before merger all configurations have SNRs of several hundreds.

It is interesting to see, in particular, how the SNR for the Hybrid configurations raises, in the left panel, as the signal sweeps up in frequency. The file containing the official ASD of CE starts from a frequency $f = 5$ Hz. Below this frequency, we can assume that CE is essentially blind. In this regime, in the Hybrid network, only the L-shaped detector with the ASD of ET contributes to the accumulation of the SNR. At $f = 5$ Hz, the surface detector with the ASD of CE kicks in, and the red and violet curves in the left panel suddenly change slope. The effect is even more visible in the right panel, where all European networks are taken together with the 40-km CE in the US, that again kicks in at 5 Hz.

Overall, for this specific event, all the networks considered in the left panel have rather similar performances among them, and this is even more the case for the configurations in the panel when adding CE. It is quite interesting to see that the accumulation of the SNR in the early part of the pre-merger phase is similar for the various network configurations, despite the fact that in the Hybrid configurations only one detector can access the low-frequency regime, while in ET-2L-mis there are two detectors that can access it, and in the 10-km triangle all three interferometers can access it. Basically, this is due to the fact that the accumulation of the SNR is dominated by the most sensitive detector in a network.

Of course, GW170817 was a very special event also because of its close distance from us, $d_L \simeq 40$ Mpc. The SNR, however, scales as $1/d_L$, so the result for a source with the same characteristics as GW170817 but at larger distance can be obtained just by rescaling the results in Figure 11. So, for a source with the same detector-frame masses, at a distance 10 times larger, i.e. about 400 Mpc, at 10^3 seconds before merger, all these configurations would still reach a SNR between 20 and 60, by itself very well sufficient for reliable detection.

Detecting a signal prior to merger is, however, only part of the story. For multi-messenger studies, we also need to get a good angular resolution before merger, in order to give to electromagnetic observatories at least some localization information, and sufficiently early. Table 6 shows the number of BNSs detected with $\text{SNR} \geq 12$ and different cuts on the sky localization, at 30 min, 10 min and 1 min prior to merger, for the various

¹⁵Recall that, by SNR, we always mean the SNR of the whole detector network, obtained combining in quadrature the SNRs of the individual detectors.

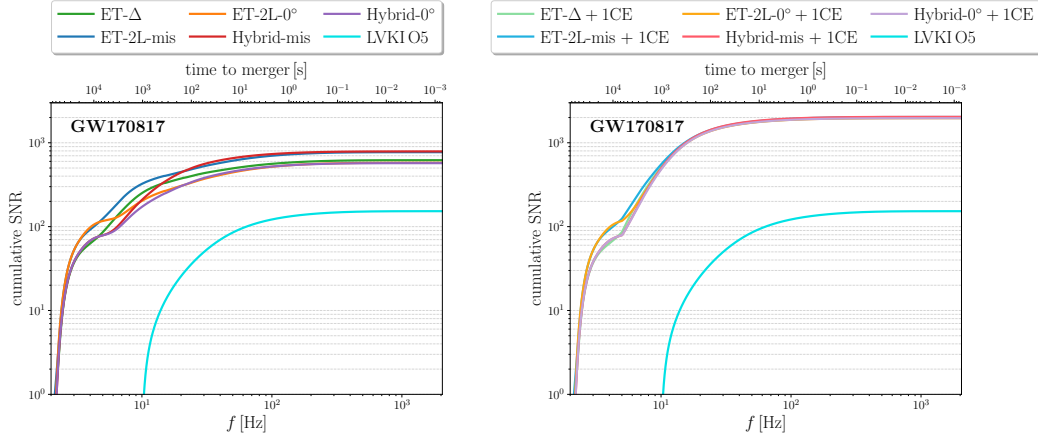


Figure 11. Accumulation of the SNR in the various 3G network configurations, for a source with the properties of the BNS GW170817, as the signal sweeps up in frequency without (*left panel*) and with (*right panel*) a single 40-km CE detector in the US. The upper horizontal scale gives the corresponding time to merger. Observe that, for this system, the merger takes place at about 2 kHz, see e.g. Figure 2 of [29].

European-only configurations studied in this work.^{16,17} We show separately the BNS detections where the orbit has a generic inclination, and those close to face-on, defined as those such that $\Theta \equiv \min\{\iota, 180^\circ - \iota\}$ is smaller than 15° , which can result more likely in coincident γ -ray burst (GRB) detections.

To illustrate these results, let us begin by discussing the events with arbitrary orbit inclination, and consider first the detections with angular resolution $\Delta\Omega_{90\%}$ smaller than 10 deg^2 . The events that are well localized have a special importance for multi-messenger astronomy because, unless some telescope devoted just to the follow-up of GW detections will be developed, realistically only a small fraction of the alerts associated to BNS signals will lead to a follow-up campaign from electromagnetic telescopes, so the best-localized events will be the natural candidates for such a follow-up. In the European-only setting, none of the configurations studied can provide such a localization 30 min or 10 min before merger. However, such a localization will be obtained for a few events 1 min before merger. In this case (within the statistical fluctuations associated to such small numbers) similar performances are obtained from ET-2L-mis, ET- Δ and Hybrid-mis, with $\{5, 4, 4\}$ events, respectively; these numbers become $\{139, 79, 76\}$ requiring $\Delta\Omega_{90\%} \leq 100 \text{ deg}^2$ at 1 min before merger; and $\{53, 28, 16\}$ for $\Delta\Omega_{90\%} \leq 100 \text{ deg}^2$ at 10 min before merger.

Observe that, for $\Delta\Omega_{90\%} \leq 100 \text{ deg}^2$, 10 min before merger ET- Δ has more events

¹⁶As in the results of the previous subsections, all these figures are for one year of data taking, with the duty cycles given at the end of Section 3.

¹⁷For ET-2L-mis and ET- Δ , these results can be compared to those in Table 3 of [17]. Note however that, there, was used a cut $\text{SNR} \geq 8$, while here we are using $\text{SNR} \geq 12$. The rationale for a lower threshold, $\text{SNR} \geq 8$, in multi-messenger studies, is that combining the GW detection with the electromagnetic detection increases the statistical significance, so the GW detection can be performed at lower SNR. However, if we are interested in providing an alert to electromagnetic observatories, the electromagnetic detection has not yet been obtained, so it can be safer to stick to $\text{SNR} \geq 12$, to avoid giving too many false alerts. In any case, the events for which one obtains the best pre-merger localization are those with high SNR, so for these events the precise value of the threshold has limited relevance. Using a higher SNR threshold also reduces the technical problems with the inversion of ill-conditioned Fisher matrices, see footnote 9 of [17].

than Hybrid-mis, 28 against 16, while 1 min before merger the performances are equivalent, with 79 events against 76. This is due to the fact that the surface detector, in the Hybrid configuration, kicks in later, but then catches up. The same pattern repeats requiring $\Delta\Omega_{90\%} \leq 1000 \text{ deg}^2$, where 10 min before merger ET- Δ has localized 125 events, to be compared with 74 for Hybrid-mis; 1 min before merger, these numbers raise to 372 and 360, respectively, therefore becoming again very similar. In any case, even at 10 min before merger, the relative performances of these two networks differ by less than a factor of 2.¹⁸

Let us focus next on the events close to face-on, $\Theta \leq 15^\circ$, for which the probability of detecting an associated GRB is higher. None of the network configurations considered, in one year of data taking, can detect such events before merger with a localization accuracy $\Delta\Omega_{90\%} \leq 10 \text{ deg}^2$, and also for $\Delta\Omega_{90\%} \leq 100 \text{ deg}^2$ there is just a handful of events in each configuration (so that the results are also more sensitive to statistical fluctuations associated to our sample of the catalog, and to random down time associated to the duty cycle). If, in order to deal with statistically more significant numbers, we rather set the cut on angular resolution at $\Delta\Omega_{90\%} \leq 1000 \text{ deg}^2$, at 10 min before merger the number of BNSs detections (again, in 1 yr of data and with our assumption for the duty cycle) with $\Theta \leq 15^\circ$ that we read from Table 6 are as follows: ET-2L-mis, 8 events; ET- Δ and ET-2L- 0° , 4 events; Hybrid-mis and Hybrid- 0° , 2 events.

We now consider the networks obtained adding also a 40-km CE in the US. The results are shown in Table 7. Now, even for $\Delta\Omega_{90\%} \leq 10 \text{ deg}^2$, at least for generic orbit inclinations, there are events localized to such accuracy even 30 or 10 min before mergers. For instance, for (ET- Δ + 1CE) we get {1, 11, 77} events localized to $\Delta\Omega_{90\%} \leq 10 \text{ deg}^2$ at, respectively, 30, 10 and 1 min before merger. For (ET-2L-mis + 1CE) we get {1, 10, 101} and, for (Hybrid-mis + 1CE), {0, 7, 103}. Requiring instead a less stringent angular localization, $\Delta\Omega_{90\%} \leq 100 \text{ deg}^2$, these numbers become, respectively: {25, 234, 2140} for (ET- Δ + 1CE); {41, 363, 2824} for (ET-2L-mis + 1CE); and {10, 159, 2730} for (Hybrid-mis + 1CE).

Overall, the conclusion is that the performances of these configurations for pre-merger alert are very comparable for the detections at about 10 min to merger and later, while, requiring a 30 min pre-alert time, (Hybrid-mis + 1CE) is less performant, by about a factor of 2.5 with respect to (ET- Δ + 1CE) and a factor of 4 with respect to (ET-2L-mis + 1CE).

4.4 Stochastic backgrounds

Finally, we consider the sensitivity to stochastic GW backgrounds (SGWBs) of these configurations. Isotropic and Gaussian stochastic backgrounds of GWs are characterized by their energy density per unit logarithmic interval of frequency, $d\rho_{\text{gw}}/d\log f$ [57, 58]. To have a dimensionless quantity, this is normalized to the critical density for closing the Universe, $\rho_c = 3H_0^2/(8\pi G)$, defining $\Omega_{\text{gw}}(f) = (1/\rho_c)d\rho_{\text{gw}}/d\log f$. Writing $H_0 = h \times (100 \text{ km s}^{-1}\text{Mpc}^{-1})$, it is then convenient to use $h^2 \Omega_{\text{gw}}(f)$ to characterize the stochastic background, to get rid of the uncertainty in h .

¹⁸The result for ET- Δ can also be compared to those in ref. [37], which obtains larger numbers: 6 and 2 events/yr with $\Delta\Omega_{90\%} \leq 10 \text{ deg}^2$ at 5 and 30 min before merger, respectively; by comparison, for $\Delta\Omega_{90\%} \leq 10 \text{ deg}^2$ we have 4 events/yr at 1 min and 0 at 30 min. However, the comparison must take into account some different assumptions. In particular, ref. [37] uses a duty cycle of 100%, while we assume an uncorrelated 85% duty cycle in each of the three detectors composing the triangle. Furthermore, ref. [37] uses the ET-D sensitivity curve, while we use a more up-to-date sensitivity curve, already used in [17], which is less good at low frequencies (see Figure 2, left panel, of [17]). Other technical differences are that ref. [37] uses full PyCBC Inference, while we restrict to Fisher matrices. The population model used is also not the same.

BNS						
Detector configuration	Time before merger	Orientation	Detections with $\Delta\Omega_{90\%} \leq$			
			10 deg ²	100 deg ²	1000 deg ²	all sky
ET- Δ	30 min	All Θ	0	8	39	345
		$\Theta \leq 15^\circ$	0	0	2	31
	10 min	All Θ	0	28	125	1 544
		$\Theta \leq 15^\circ$	0	2	4	153
	1 min	All Θ	4	79	372	7 599
		$\Theta \leq 15^\circ$	0	3	9	767
ET-2L-mis	30 min	All Θ	0	19	83	807
		$\Theta \leq 15^\circ$	0	0	3	78
	10 min	All Θ	0	53	288	3 439
		$\Theta \leq 15^\circ$	0	3	8	308
	1 min	All Θ	5	139	697	14 765
		$\Theta \leq 15^\circ$	0	5	22	1 562
ET-2L-0 $^\circ$	30 min	All Θ	0	4	50	818
		$\Theta \leq 15^\circ$	0	0	2	78
	10 min	All Θ	0	11	117	3 458
		$\Theta \leq 15^\circ$	0	1	4	311
	1 min	All Θ	2	25	323	14 991
		$\Theta \leq 15^\circ$	0	0	13	1 593
Hybrid-mis	30 min	All Θ	0	2	16	354
		$\Theta \leq 15^\circ$	0	0	0	28
	10 min	All Θ	0	16	74	1 686
		$\Theta \leq 15^\circ$	0	0	2	159
	1 min	All Θ	4	76	360	12 075
		$\Theta \leq 15^\circ$	0	3	13	1 185
Hybrid-0 $^\circ$	30 min	All Θ	0	0	8	354
		$\Theta \leq 15^\circ$	0	0	0	27
	10 min	All Θ	0	4	36	1 704
		$\Theta \leq 15^\circ$	0	0	2	162
	1 min	All Θ	1	12	167	12 219
		$\Theta \leq 15^\circ$	0	0	4	1 190

Table 6. Number of BNS detected with $\text{SNR} \geq 12$ and different cuts on the sky localization at 30 min, 10 min and 1 min prior to merger for the various European-only configurations studied in this work. We further report the numbers both for all the sources in the catalog and the sub-sample of sources having an angle $\Theta \leq 15^\circ$, which can result more likely in coincident GRB detections.

The sensitivity to stochastic background can be expressed in terms of the power-law integrated sensitivity (PLS) introduced in [59] (see also App. A of [17] for conventions and

BNS						
Detector configuration	Time before merger	Orientation	Detections with $\Delta\Omega_{90\%} \leq$			
			10 deg ²	100 deg ²	1000 deg ²	all sky
ET- Δ + 1CE	30 min	All Θ	1	25	229	418
		$\Theta \leq 15^\circ$	0	0	5	37
	10 min	All Θ	11	234	1888	2493
		$\Theta \leq 15^\circ$	0	9	64	233
	1 min	All Θ	77	2140	22906	33042
		$\Theta \leq 15^\circ$	3	76	790	3136
ET-2L-mis + 1CE	30 min	All Θ	1	41	307	875
		$\Theta \leq 15^\circ$	0	0	9	82
	10 min	All Θ	10	363	2521	4542
		$\Theta \leq 15^\circ$	0	10	79	417
	1 min	All Θ	101	2824	27880	42804
		$\Theta \leq 15^\circ$	7	82	909	4057
ET-2L-0 ^o + 1CE	30 min	All Θ	1	19	195	885
		$\Theta \leq 15^\circ$	0	0	3	86
	10 min	All Θ	3	100	1080	4540
		$\Theta \leq 15^\circ$	0	1	41	426
	1 min	All Θ	29	627	6844	42977
		$\Theta \leq 15^\circ$	0	21	220	4063
Hybrid-mis + 1CE	30 min	All Θ	0	10	149	416
		$\Theta \leq 15^\circ$	0	0	4	36
	10 min	All Θ	7	159	1577	2655
		$\Theta \leq 15^\circ$	1	6	48	254
	1 min	All Θ	103	2730	25179	39062
		$\Theta \leq 15^\circ$	5	85	867	3591
Hybrid-0 ^o + 1CE	30 min	All Θ	0	7	101	417
		$\Theta \leq 15^\circ$	0	0	0	36
	10 min	All Θ	2	56	614	2681
		$\Theta \leq 15^\circ$	0	5	29	259
	1 min	All Θ	24	458	5177	39221
		$\Theta \leq 15^\circ$	0	22	196	3605

Table 7. As in Table 6, for the networks including a 40-km CE in the US.

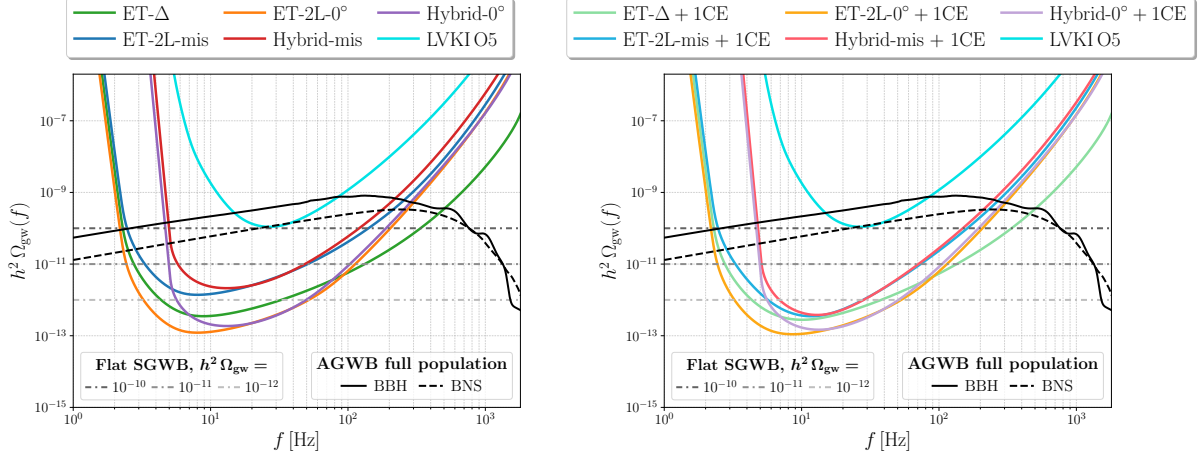


Figure 12. Power-law integrated sensitivity curves for $h^2 \Omega_{\text{gw}}(f)$ for the various configurations studied without (*left panel*) and with (*right panel*) a single 40-km CE detector in the US. These are computed assuming an observational time $T_{\text{obs}} = 1$ yr and an SNR threshold of 1. We further report some SGWB examples, namely a flat-in-frequency background with different amplitudes and the AGWB generated by our 1 yr catalogs of BBHs and BNSs.

definitions). [Figure 12](#) shows the PLS of the various network configurations studied, expressed in terms of $h^2 \Omega_{\text{gw}}(f)$. We see that, at high frequencies (above about 100 Hz), the 10-km triangle provides the best sensitivity. This is due to the fact that, for colocated detectors, there is almost no suppression from the overlap reduction function which instead, for two detectors at a distance d , suppresses the correlation when $fd/c \gg 1$ (see e.g. [\[58\]](#)).¹⁹ We also observe that, going toward low-frequencies, the Hybrid configurations hit a sensitivity wall earlier, compared to the ET- Δ or ET-2L. This is due to the fact that stochastic backgrounds are measured by correlating the output of two detectors so, in a two-detector correlation, the result is dominated by the less sensitive detector, and below ~ 5 Hz, where the surface detector with the ASD of CE becomes blind, the whole Hybrid networks also become blind to stochastic backgrounds.²⁰

For the same reasons, adding a CE in the US (*right panel*) does not improve the sensitivity below 5 Hz, and also has a limited effect at large frequencies, because of the long baseline d between US and European detectors, and the corresponding suppression due to the overlap reduction function. In general, adding a CE in the US has limited effect in the whole frequency range for ET- Δ and for the Hybrid- 0° and ET-2L- 0° configurations; this is due to the fact that in any case, because of the suppression by the overlap reduction function, the correlation between a detector in the US and detectors in Europe is less good, compared to what can be achieved for stochastic backgrounds by well-correlated 3G detectors in Europe. However, between about 10 Hz and a few hundred Hz, adding a CE in the US improves significantly the performances of the Hybrid-mis and ET-2L-mis networks,

¹⁹Of course, the reverse of the coin is that, for colocated detectors, there will be a larger correlated noise (particularly at low frequencies), that would simulate a stochastic GW background, see [\[60, 61\]](#) and Section 5.4.1 of [\[17\]](#). The PLS in [Figure 12](#), as well as the corresponding SNR for various signals reported below, are computed assuming that the noise in the different detectors are uncorrelated.

²⁰Note that this is different from what we found in [Section 4.3](#) for the accumulation of the SNR in the pre-merger phase. Indeed, in that case the result was dominated by the most sensitive detector in the low-frequency region, so having just one detector sensitive to the low frequencies was sufficient.

Detector configuration	SNR for				
	flat SGWB, $h^2 \Omega_{\text{gw}} =$			AGWB	
	10^{-10}	10^{-11}	10^{-12}	all BBH	all BNS
ET- Δ	285.2	28.5	2.9	621.6	174.5
ET-2L-mis	72.1	7.2	0.7	148.6	41.3
ET-2L-0 $^\circ$	821.4	82.1	8.2	1 693.7	470.6
Hybrid-mis	47.1	4.7	0.5	126.6	36.8
Hybrid-0 $^\circ$	536.1	53.6	5.4	1 439.2	417.8

Table 8. SNRs at the various European configurations for different stochastic background sources in an observational time $T_{\text{obs}} = 1$ yr. The columns 2, 3 and 4 show the results for a flat-in-frequency SGWB with different amplitudes, the fifth and sixth column for the superposition of all the BBH and BNS signals present in our 1 yr catalogs, respectively.

Detector configuration	SNR for				
	flat SGWB, $h^2 \Omega_{\text{gw}} =$			AGWB	
	10^{-10}	10^{-11}	10^{-12}	all BBH	all BNS
ET- Δ + 1CE	358.8	35.9	3.6	828.7	234.9
ET-2L-mis + 1CE	285.3	28.5	2.9	698.7	199.7
ET-2L-0 $^\circ$ + 1CE	909.2	90.9	9.1	1 948.3	545.3
Hybrid-mis + 1CE	263.0	26.3	2.6	677.7	195.3
Hybrid-0 $^\circ$ + 1CE	679.4	67.9	6.8	1 807.2	523.6

Table 9. As in [Table 8](#), adding to each network a single 40-km CE detector in the US.

where the relative orientation between the two European L-shaped detectors suppresses the sensitivity to stochastic backgrounds, and therefore adding one more detector, not parallel, has a significant effect.

As we see from [Figure 12](#), the relative performances of some configurations depend on the frequency range. For instance, comparing the PLS of ET-2L-0 $^\circ$ and ET- Δ , we see that the former is better for f below about 100 Hz, and the latter is better above 100 Hz. Comparing ET- Δ to Hybrid-0 $^\circ$, we see that ET- Δ is better below about 8; then, from 8 to 80 Hz, is better Hybrid-0 $^\circ$; and above 80 Hz is better again ET- Δ . The SNR of a given stochastic background signal $h^2 \Omega_{\text{gw}}(f)$ is a quantity integrated over the frequencies, so in the end which configuration will perform better depends on the shape of the signal in frequency. To obtain a more quantitative understanding, we consider some examples of possible signals, also shown in [Figure 12](#):

- (1) A stochastic background where $h^2 \Omega_{\text{gw}}$ is flat in frequency, and chosen to have the values 10^{-10} , 10^{-11} , or 10^{-12} . Signals for which $h^2 \Omega_{\text{gw}}$ is approximately constant in f , at least over the range of frequencies explored by ground-based GW detectors, emerge rather naturally in cosmology, where typical spectra extend over many more decades in frequency, and the range explored by ground-based detectors is comparatively small. An explicit example is provided by some models for cosmic strings, see e.g. [Figure 63](#)

of [17].²¹

- (2) The current best estimate of the astrophysical GW background (AGWB) obtained from the superposition of all BBH signals, and that obtained from all BNS signals. We compute it as in Section 5.3 of [17].²²

The SNR for a given stochastic background signal is then computed as in Section 7.8.3 of [68]. The results for the European-only networks are shown in Table 8. We see that, for these spectra, the best results come from ET-2L-0° followed by Hybrid-0°. These perform clearly better than ET-Δ which, in turn, performs clearly better than ET-2L-mis and Hybrid-mis. Table 9 shows the results when adding also the 40-km CE in the US. We see that the hierarchy between the configurations remains the same, and ET-2L-0° and Hybrid-0° are still clearly the best configurations. However, now the performances of ET-2L-mis and Hybrid-mis become quite comparable to that of ET-Δ.

The signals considered in Figure 12 and Tables 8 and 9 are either flat or only mildly varying with frequency, within the detector’s bandwidth. It is also interesting to compute the SNR for signals with a stronger frequency dependence. We then consider a power-law spectrum

$$\Omega_{\text{gw}}(f) = \Omega_0 \left(\frac{f}{f_0} \right)^\alpha, \quad (4.1)$$

where f_0 is a reference frequency such that $\Omega_{\text{gw}}(f_0)$ has the value Ω_0 , and we consider a very steep “blue” spectrum with $\alpha = 3$ (such spectra could for instance emerge for instance in the context of pre-big-bang models [69–71]), and a “red” spectrum with $\alpha = -1$ (this could emerge, in particular, in the stochastic background generated by bubble collisions at frequencies above the peak of the spectrum; see Section 22.4.4 of [62]). In both cases we set the reference frequency to the value $f_0 = 10$ Hz; for $\alpha = 3$ we then consider the cases $h^2\Omega_0 = \{10^{-12}, 10^{-13}, 10^{-14}\}$, while for $\alpha = -1$ we consider the cases $h^2\Omega_0 = \{10^{-10}, 10^{-11}, 10^{-12}\}$. These spectra are shown in Figure 13, together with the PLS of the various configuration. The corresponding values of the SNR are given in Tables 10 and 11. Blue spectra are more sensitive to the PLS at high frequency, and therefore for them the relative performance of the triangle with respect to 2L improves. So, for instance, we saw from Table 8 that, for a flat background, the SNR of the Hybrid-0° configuration is almost a factor of 2 larger than the SNR for ET-Δ (and that of ET-2L-0° is larger than that of ET-Δ by a factor about 3); in contrast, from Table 10, we see that for a steep blue spectrum with $\alpha = 3$ the SNR of the triangle is larger than that of Hybrid-0° by a factor of about 3 (and is larger than that of ET-2L-0° by a factor of about 2).

²¹The stochastic background produced by the amplification of vacuum fluctuations in single-field slow-roll inflation is also almost flat in $h^2\Omega_{\text{gw}}$, at the frequencies of ground-based detectors. Unfortunately, at the frequencies of 3G ground-based detectors, or of LISA, it gives a prediction for $h^2\Omega_{\text{gw}}$ which is at most 10^{-16} (see e.g. Figure 21.9 of [62]) and therefore is not detectable, neither by 3G ground based detectors nor by LISA.

²²Observe that, at a given detector network, some of these signals from compact binaries will be resolved, while those below detection threshold, together also with the error in the subtraction of the resolved sources, will form a stochastic background [63–67]. This residual background is of course dependent on the detector network. For instance, at an ideal detector network that would resolve all sources, and subtract them with no error, no residual background would be left. To compare the PLS with some example of signals, it is therefore more meaningful to consider the full AGWB generated by the superposition of all sources, resolved or unresolved.

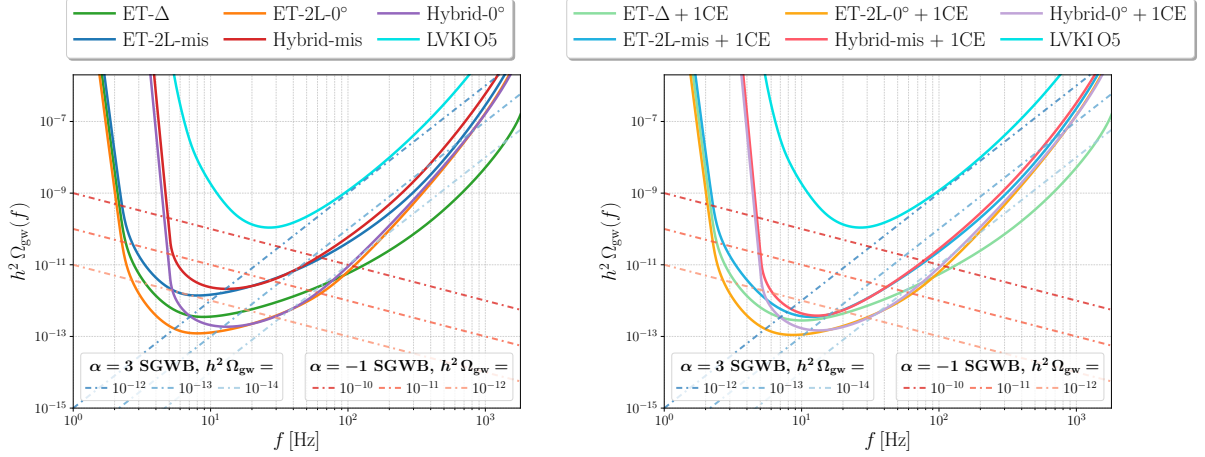


Figure 13. The same PLS shown in Fig. 12, now compared to power law signals $\Omega_{\text{gw}}(f) = \Omega_0 (f/f_0)^\alpha$ with $\alpha = 3$ and $\alpha = -1$ and different amplitudes.

Detector configuration	SNR for					
	$\alpha = 3, h^2\Omega_0 =$			$\alpha = -1, h^2\Omega_0 =$		
	10^{-12}	10^{-13}	10^{-14}	10^{-10}	10^{-11}	10^{-12}
ET- Δ	385.5	38.6	3.9	374.0	37.4	3.7
ET-2L-mis	29.4	2.9	0.3	103.5	10.3	1.0
ET-2L-0 $^\circ$	166.5	16.7	1.7	1178.1	117.8	11.8
Hybrid-mis	17.7	1.8	0.2	42.7	4.3	0.4
Hybrid-0 $^\circ$	130.6	13.1	1.3	486.0	48.6	4.9

Table 10. SNRs at the various European configurations for different stochastic background sources in an observational time $T_{\text{obs}} = 1$ yr, for the power-law spectra given in eq. (4.1), with $f_0 = 10$ Hz and different values of Ω_0 and α .

Detector configuration	SNR for					
	$\alpha = 3, h^2\Omega_0 =$			$\alpha = -1, h^2\Omega_0 =$		
	10^{-12}	10^{-13}	10^{-14}	10^{-10}	10^{-11}	10^{-12}
ET- Δ + 1CE	386.2	38.6	3.9	420.5	42.0	4.2
ET-2L-mis + 1CE	42.8	4.3	0.4	278.9	27.9	2.8
ET-2L-0 $^\circ$ + 1CE	171.5	17.1	1.7	1233.1	123.3	12.3
Hybrid-mis + 1CE	36.2	3.6	0.4	228.2	22.8	2.3
Hybrid-0 $^\circ$ + 1CE	136.6	13.7	1.4	591.0	59.1	5.9

Table 11. As in Table 10, adding to each network a single 40-km CE detector in the US.

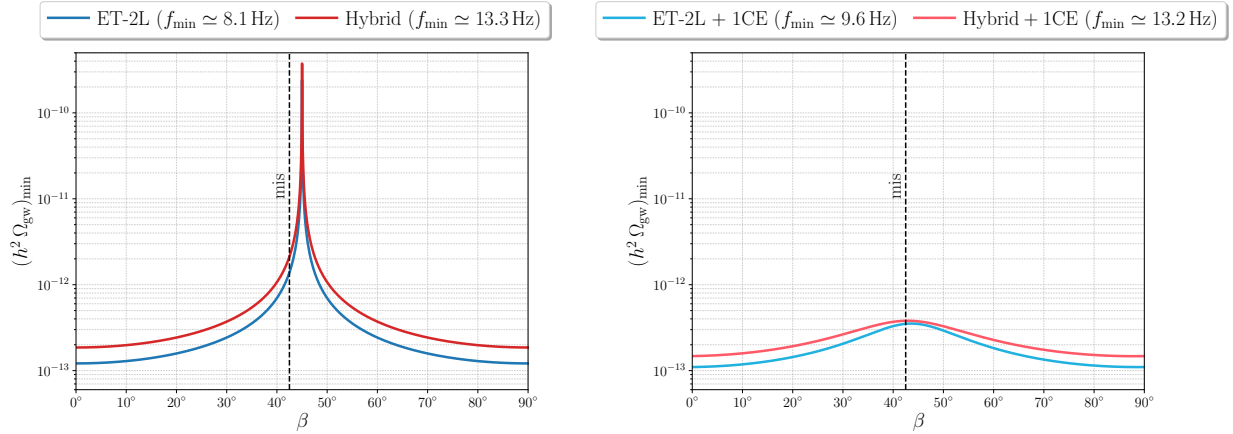


Figure 14. Minimum value attained by the PLS for $h^2 \Omega_{\text{gw}}(f)$, as a function of the relative angle β between the European L-shaped detectors, for the ET-2L and Hybrid configurations, without (*left panel*) and with (*right panel*) a single 40-km CE detector in the US (whose orientation is kept fixed). In each panel, the black dashed line denote the alignment corresponding to the “mis” configuration considered in the present work. The frequency where the PLS attains its minimum is shown in the legend.

Again, it should be stressed that these results are obtained assuming that the noise in the different detectors are uncorrelated, an assumption which is more delicate for the colocated interferometers in the ET- Δ configuration.

Finally, for the configurations involving two L-shaped detectors, it is interesting to understand how the results depend on the relative orientation of the two Ls. [Figure 14](#) shows how the minimum value of the PLS depends on the angle β defined in [Section 2](#) with reference to the great circle connecting the two detectors. As discussed in [Section 2](#), for a network of two L-shaped detectors at a distance d , in the limit $d/\lambda \rightarrow 0$ (where $\lambda = c/f$ is the GW wavelength) the sensitivity goes to zero for $\beta = 45^\circ$; indeed, we see from the left panel of [Figure 14](#) that, for this angle, the minimum of the PLS becomes large (not strictly infinity, given that the detectors are not colocated). The misaligned configurations that we have studied correspond to the value of β marked by the vertical dashed line in the figure. We see that it is quite close to the value where the sensitivity to stochastic background is the worst. However, a somewhat larger misalignment angle would not significantly affect the performances for coalescing binaries, while we see from the figure that it would give a non-negligible improvement to the sensitivity to stochastic backgrounds.

Having three L-shaped detectors, as in the (ET-2L + 1CE) and (Hybrid-2L + 1CE) configurations, also allows us to play with all the relative angles, to optimize both the sensitivity to coalescing binaries and to stochastic backgrounds. In particular, one could set the two European L-shaped detectors close to parallel, and the US detector close to 45° to them. Putting at 45° the detectors that have a large baseline optimizes the sensitivity to parameter estimation of coalescing binaries (in particular, angular localization), while setting parallel the two European detectors, that have the shorter baseline, is the best way of optimizing the sensitivity to stochastic backgrounds. Eventually, if one of these configurations should be implemented, dedicated study of the optimization of the science output as a function of the relative orientation angles will be necessary.

5 Conclusions

In this paper we have studied the performance of a hypothetical European detector network made by a surface detector and an underground detector. For the underground detector we have considered a single L-shaped detector with the ASD of ET (therefore featuring a high-frequency and a low-frequency interferometer), taken to have 15 km arms. For the detector on-surface we have “borrowed” the ASD of CE with 20 km arms but, as we stressed in the Introduction, this choice is only made for simplicity, since the ASD of CE is the only publicly available curve for a 3G surface detector.

We have then compared this “Hybrid” configuration to the two options for ET that are currently under active investigation, namely a single-site 10-km triangle, or two 15-km L-shaped underground detectors in different European sites. We have compared these three networks among them, and we have further compared them when, to each of these networks, is added a 40-km CE detector in the US.

The motivation that inspired this work is that of extending the study of the performance of a third-generation observatory to configurations not previously considered. The results presented here therefore go in the direction of completing the picture of the capabilities of various configurations using 3G detectors whose individual performances have already been presented in literature. From here the interest to understand what one can do by correlating a single L-shaped interferometer with the characteristics of ET, with a second interferometer built on the Earth’s surface rather than underground, and not requiring the “xylophone” configuration with a low-frequency cryogenic instrument.

In the context of a European-only network, our main results are as follows:

- For the detection horizons, above about $30 M_{\odot}$ all these 3G configurations are very similar, but below there are significant differences, and ET-2L-mis and Hybrid-mys are superior to ET- Δ . For instance, for the total mass typical of BNS, $M_{\text{tot}} = 2.7 M_{\odot}$, ET- Δ has a detection horizon $z_{\text{hor}} \simeq 3.3$, while the Hybrid configurations and the ET-2L configurations both have $z_{\text{hor}} \simeq 5.3$; see the left panel of [Figure 2](#) and the left table in [Table 1](#). Similarly considerations hold for coalescing binaries with subsolar masses, that would be a smoking-gun signature of primordial black holes; e.g., for $M_{\text{tot}} = 1.0 M_{\odot}$, ET- Δ has a detection horizon $z_{\text{hor}} \simeq 1.0$, while the Hybrid configurations and the ET-2L configurations have $z_{\text{hor}} \simeq 1.4$. In terms of comoving volumes, between $z = 1.4$ and $z = 1.0$ there is a factor 2.0, which would reflect in the probability of primordial black holes detection.
- For BBHs, the configurations ET-2L-mis and Hybrid-mys are clearly superior to ET- Δ for SNR distribution, angular localization, and reconstruction of the luminosity distance, see [Figures 3](#) and [4](#), and [Table 2](#).
- For BNS, for angular localization the best configuration is ET-2L-mis, followed by ET-2L- 0° and Hybrid-mys, which in turn are superior to ET- Δ and Hybrid- 0° . For luminosity distance, ET-2L-mis is again clearly the best, followed by Hybrid-mys. See [Figures 5](#) and [6](#), and [Table 2](#).
- For pre-merger alerts, the left panel of [Figure 11](#) shows that, for a GW170817-like event, the SNR accumulates before merger in a rather similar manner between the different 3G configurations considered. For the angular localization before merger, we see from [Table 6](#) that all these 3G configurations have comparable performances at 10 min to

merger or later; at a finer level, ET-2L-mis is somewhat better than ET- Δ and Hybrid-mis, which are very similar among them, within a factor less than 2. At 30 min before merger, however, Hybrid-mis is less performant than ET- Δ , by a factor between 2 and 4 in the number of events with a given localization.

- The sensitivities to stochastic backgrounds of the various configurations of European-only networks are shown in the left panel of [Figure 12](#), and the corresponding SNR for some examples of stochastic backgrounds are given in [Table 8](#) and [Table 10](#). As we see from [Table 8](#), for flat or almost flat backgrounds the best configurations in general are ET-2L-0° and Hybrid-0°, which are better than ET- Δ , which in turn is better than ET-2L-mis and Hybrid-mis. However, for steep blue spectra, the ET- Δ configurations becomes the best one, while for red spectra the ET-2L-0° is the best one, see [Table 10](#). It should also be observed that, in the 2L case, the results for the misaligned configurations are quite specific to our choice of misalignment angle; the sensitivity to stochastic background of these configurations could be improved by increasing this misalignment angle which, to some extent, can be done without significantly affecting the performance for parameter estimation of coalescing binaries.

It should also be stressed that we have computed the sensitivity to stochastic backgrounds by correlating the outputs of pairs of detectors, and exploiting the fact that the GW signal is correlated, while assuming that the noise is uncorrelated. This assumption is never totally correct, but this could be a particularly serious concern for the colocated interferometers of the triangle configuration, in particular at low frequencies, where seismic and Newtonian noise induce correlated noise among the colocated interferometers of the triangle.

When we put these European configurations in a broader world-wide network with a 40-km CE in the US, the hierarchy of performances among the configurations remains the same, but the relative differences between them become much less important. In particular:

- The detection horizons becomes practically identical, see the right panel of [Figure 2](#) and the right panel in [Table 1](#).
- The SNR distribution and parameter estimation for BBHs becomes very similar for all configurations, with differences in the number of events with given cuts that, among all configurations, do not exceed a factor of 2, with (ET-2L-mis + 1CE) and (Hybrid-mis + 1CE) being the best configurations; see [Figures 7](#) and [8](#), and [Table 4](#).
- For BNSs the spread in the results between configurations is slightly larger than for BBHs but still, among all configurations, it does not exceed a factor of about 3.5 between the best and the less good configuration; again, (ET-2L-mis + 1CE) is the best configuration and (Hybrid-mis + 1CE) is the second best; see [Figures 9](#) and [10](#), and [Table 5](#).
- For pre-merger alerts, the performances of all configurations are comparable; the best configuration is again (ET-2L-mis + 1CE), but (ET- Δ + 1CE) and (ET-2L-0° + 1CE) follow very closely; for alerts at 30 min before merger the (Hybrid + 1CE) configurations are less performant, but they partially catch up for alert at 10 min or less before merger. For instance, the number of BNS localized to better than 100 deg^2 , 30 min before merger, for (ET- Δ + 1CE), (ET-2L-mis + 1CE), (ET-2L-0° + 1CE), (Hybrid-mis

+ 1CE) and (Hybrid-0° + 1CE) are, respectively, {25, 41, 19, 10, 7}; at 10 min before merger, these numbers become, respectively, {234, 363, 100, 159, 56}; see the right panel of Table 7. Figure 11 shows how the SNR accumulates in an event such as GW170817, and for such an event the differences between configurations are marginal.

- The sensitivities of the various configurations to stochastic backgrounds are shown in the right panel of Figure 12, and the corresponding SNR of some example of stochastic backgrounds are given in Table 9. For instance, for the astrophysical background due to the superposition of BBHs, Table 9 gives the SNR values {829, 699, 1948, 678, 1807}, respectively for ET- Δ , ET-2L-mis, ET-2L-0°, Hybrid-mis and Hybrid-0° (each one together with 1CE). Similar results hold for the other stochastic backgrounds considered. The best configurations are therefore now (ET-2L-0° + 1CE) and (Hybrid-0° + 1CE), but the results for the SNR differ by less than a factor of 3 between the best and the less good configuration. In a direct comparison between (ET- Δ + 1CE) and (Hybrid-mis + 1CE), we see that the SNR for this background are 829 for (ET- Δ + 1CE) and 678 for (Hybrid-mis + 1CE), a difference of less than 20%. The same holds for the other stochastic backgrounds considered.

These results could be a useful input to an analysis of the costs and risks of different detector configurations. We stress again that the specific choice that we made for the location of a surface detector in Spain does not correspond to any project currently under study from the many points of view (geological, topographical, financial, political, etc.) that are necessary for determining viable detector configurations and optimal site selection, and that the “hybrid” configuration that we have studied, with an underground L-shaped detector with the ASD of ET and an on-surface 3G detector, does not correspond to any project currently endorsed by the ET Collaboration. This work should be considered as an investigation with the purpose of understanding better what builds up the sensitivity of a GW network.

Acknowledgements

We thank Eugenio Coccia and Mario Martinez for very valuable discussions that inspired this study. We also thank Giancarlo Cella, Jerome Degallaix, Ik Siong Heng, Mikhail Korobko and Andrea Maselli for their very useful internal ET review.

The work of F.I., M.Mag. and N.M. is supported by the Swiss National Science Foundation (SNSF) grants 200020_191957 and by the SwissMap National Center for Competence in Research. E.B. and M.Mag. are supported by the SNSF grant CRSII5_213497. M.Mag. thanks for the hospitality the IFAE in Barcelona, where part of this work was done. The work of M.Manc. received support from the French government under the France 2030 investment plan, as part of the Initiative d’Excellence d’Aix-Marseille Université – A*MIDEX AMX-22-CEI-02. This work made use of the clusters Yggdrasil and Baobab at the University of Geneva.

References

- [1] **LIGO Scientific, Virgo** Collaboration, B. P. Abbott *et al.*, “Observation of Gravitational Waves from a Binary Black Hole Merger,” *Phys. Rev. Lett.* **116** no. 6, (2016) 061102, [arXiv:1602.03837](https://arxiv.org/abs/1602.03837) [gr-qc].

- [2] **LIGO Scientific, Virgo** Collaboration, B. P. Abbott *et al.*, “GW170817: Observation of Gravitational Waves from a Binary Neutron Star Inspiral,” *Phys. Rev. Lett.* **119** no. 16, (2017) 161101, [arXiv:1710.05832 \[gr-qc\]](#).
- [3] **LIGO Scientific, Virgo, Fermi-GBM, INTEGRAL** Collaboration, B. P. Abbott *et al.*, “Gravitational Waves and Gamma-rays from a Binary Neutron Star Merger: GW170817 and GRB 170817A,” *Astrophys. J. Lett.* **848** no. 2, (2017) L13, [arXiv:1710.05834 \[astro-ph.HE\]](#).
- [4] **LIGO Scientific, Virgo, Fermi GBM, INTEGRAL, IceCube, AstroSat Cadmium Zinc Telluride Imager Team, IPN, Insight-Hxmt, ANTARES, Swift, AGILE Team, 1M2H Team, Dark Energy Camera GW-EM, DES, DLT40, GRAWITA, Fermi-LAT, ATCA, ASKAP, Las Cumbres Observatory Group, OzGrav, DWF (Deeper Wider Faster Program), AST3, CAASTRO, VINROUGE, MASTER, J-GEM, GROWTH, JAGWAR, CaltechNRAO, TTU-NRAO, NuSTAR, Pan-STARRS, MAXI Team, TZAC Consortium, KU, Nordic Optical Telescope, ePESSTO, GROND, Texas Tech University, SALT Group, TOROS, BOOTES, MWA, CALET, IKI-GW Follow-up, H.E.S.S., LOFAR, LWA, HAWC, Pierre Auger, ALMA, Euro VLBI Team, Pi of Sky, Chandra Team at McGill University, DFN, ATLAS Telescopes, High Time Resolution Universe Survey, RIMAS, RATIR, SKA South Africa/MeerKAT** Collaboration, B. P. Abbott *et al.*, “Multi-messenger Observations of a Binary Neutron Star Merger,” *Astrophys. J. Lett.* **848** no. 2, (2017) L12, [arXiv:1710.05833 \[astro-ph.HE\]](#).
- [5] **LIGO Scientific, Virgo** Collaboration, R. Abbott *et al.*, “GWTC-2: Compact Binary Coalescences Observed by LIGO and Virgo During the First Half of the Third Observing Run,” *Phys. Rev. X* **11** (2021) 021053, [arXiv:2010.14527 \[gr-qc\]](#).
- [6] **LIGO Scientific, VIRGO, KAGRA** Collaboration, R. Abbott *et al.*, “GWTC-3: Compact Binary Coalescences Observed by LIGO and Virgo During the Second Part of the Third Observing Run,” [arXiv:2111.03606 \[gr-qc\]](#).
- [7] **LIGO Scientific, VIRGO, KAGRA** Collaboration, R. Abbott *et al.*, “The population of merging compact binaries inferred using gravitational waves through GWTC-3,” [arXiv:2111.03634 \[astro-ph.HE\]](#).
- [8] **LIGO Scientific, VIRGO, KAGRA** Collaboration, R. Abbott *et al.*, “Tests of General Relativity with GWTC-3,” [arXiv:2112.06861 \[gr-qc\]](#).
- [9] **LIGO Scientific, VIRGO, KAGRA** Collaboration, R. Abbott *et al.*, “Constraints on the cosmic expansion history from GWTC-3,” [arXiv:2111.03604 \[astro-ph.CO\]](#).
- [10] M. Punturo *et al.*, “The Einstein Telescope: A third-generation gravitational wave observatory,” *Class. Quant. Grav.* **27** (2010) 194002.
- [11] S. Hild *et al.*, “Sensitivity Studies for Third-Generation Gravitational Wave Observatories,” *Class. Quant. Grav.* **28** (2011) 094013, [arXiv:1012.0908 \[gr-qc\]](#).
- [12] M. Maggiore *et al.*, “Science Case for the Einstein Telescope,” *JCAP* **2003** (2020) 050, [arXiv:1912.02622 \[astro-ph.CO\]](#).
- [13] D. Reitze *et al.*, “Cosmic Explorer: The U.S. Contribution to Gravitational-Wave Astronomy beyond LIGO,” *Bull. Am. Astron. Soc.* **51** no. 7, (2019) 035, [arXiv:1907.04833 \[astro-ph.IM\]](#).
- [14] M. Evans *et al.*, “A Horizon Study for Cosmic Explorer: Science, Observatories, and Community,” [arXiv:2109.09882 \[astro-ph.IM\]](#).
- [15] M. Evans *et al.*, “Cosmic Explorer: A Submission to the NSF MPSAC ngGW Subcommittee,” (6, 2023) , [arXiv:2306.13745 \[astro-ph.IM\]](#).
- [16] S. Borhanian and B. S. Sathyaprakash, “Listening to the Universe with Next Generation Ground-Based Gravitational-Wave Detectors,” [arXiv:2202.11048 \[gr-qc\]](#).

- [17] M. Branchesi *et al.*, “Science with the Einstein Telescope: a comparison of different designs,” *JCAP* **07** (2023) 068, [arXiv:2303.15923 \[gr-qc\]](#).
- [18] I. Gupta *et al.*, “Characterizing Gravitational Wave Detector Networks: From A[#] to Cosmic Explorer,” [arXiv:2307.10421 \[gr-qc\]](#).
- [19] A. Puecher, A. Samajdar, and T. Dietrich, “Measuring tidal effects with the Einstein Telescope: A design study,” *Phys. Rev. D* **108** no. 2, (2023) 023018, [arXiv:2304.05349 \[astro-ph.IM\]](#).
- [20] S. Bhagwat, C. Pacilio, P. Pani, and M. Mapelli, “Landscape of stellar-mass black-hole spectroscopy with third-generation gravitational-wave detectors,” *Phys. Rev. D* **108** no. 4, (2023) 043019, [arXiv:2304.02283 \[gr-qc\]](#).
- [21] G. Franciolini, F. Iacovelli, M. Mancarella, M. Maggiore, P. Pani, and A. Riotto, “Searching for primordial black holes with the Einstein Telescope: Impact of design and systematics,” *Phys. Rev. D* **108** no. 4, (2023) 043506, [arXiv:2304.03160 \[gr-qc\]](#).
- [22] F. Iacovelli, M. Mancarella, C. Mondal, A. Puecher, T. Dietrich, F. Gulminelli, M. Maggiore, and M. Oertel, “Nuclear physics constraints from binary neutron star mergers in the Einstein Telescope era,” *Phys. Rev. D* **108** no. 12, (2023) 122006, [arXiv:2308.12378 \[gr-qc\]](#).
- [23] P. Jaranowski, A. Krolak, and B. F. Schutz, “Data analysis of gravitational - wave signals from spinning neutron stars. 1. The Signal and its detection,” *Phys. Rev. D* **58** (1998) 063001, [arXiv:gr-qc/9804014](#).
- [24] L. Barsotti, E. Calloni, H. Grote, C. Olivetto, P. Rapagnani, A. Rocchi, B. Swinkels, M. Tacca, E. Tournefier, and B. Willke, “Report of the Einstein Telescope Risk Assessment Committee.” Internal ET report, 2023.
- [25] E. E. Flanagan, “The Sensitivity of the laser interferometer gravitational wave observatory (LIGO) to a stochastic background, and its dependence on the detector orientations,” *Phys. Rev. D* **48** (1993) 2389–2407, [arXiv:astro-ph/9305029](#).
- [26] N. Christensen, “Optimal detection strategies for measuring the stochastic gravitational radiation background with laser interferometric antennas,” *Phys. Rev. D* **55** (1997) 448–454.
- [27] **KAGRA, LIGO Scientific, Virgo, VIRGO** Collaboration, B. P. Abbott *et al.*, “Prospects for observing and localizing gravitational-wave transients with Advanced LIGO, Advanced Virgo and KAGRA,” *Living Reviews in Relativity* **23** no. 1, (Sept., 2020) 3, [arXiv:1304.0670 \[gr-qc\]](#).
- [28] S. Borhanian, “GWBENCH: a novel Fisher information package for gravitational-wave benchmarking,” *Class. Quant. Grav.* **38** (2021) 175014, [arXiv:2010.15202 \[gr-qc\]](#).
- [29] F. Iacovelli, M. Mancarella, S. Foffa, and M. Maggiore, “Forecasting the detection capabilities of third-generation gravitational-wave detectors using GWFAST,” *Astrophys. J.* **941** no. 2, (2022) 208, [arXiv:2207.02771 \[gr-qc\]](#).
- [30] F. Iacovelli, M. Mancarella, S. Foffa, and M. Maggiore, “GWFAST: a Fisher information matrix Python code for third-generation gravitational-wave detectors,” *Astrophys. J. Suppl.* **263** (2022) 2, [arXiv:2207.06910 \[astro-ph.IM\]](#).
- [31] U. Dupletsa, J. Harms, B. Banerjee, M. Branchesi, B. Goncharov, A. Maselli, A. C. S. Oliveira, S. Ronchini, and J. Tissino, “gwfish: A simulation software to evaluate parameter-estimation capabilities of gravitational-wave detector networks,” *Astron. Comput.* **42** (2023) 100671, [arXiv:2205.02499 \[gr-qc\]](#).
- [32] M. L. Chan, C. Messenger, I. S. Heng, and M. Hendry, “Binary Neutron Star Mergers and Third Generation Detectors: Localization and Early Warning,” *Phys. Rev. D* **97** (2018) 123014, [arXiv:1803.09680 \[astro-ph.HE\]](#).
- [33] Y. Li, I. S. Heng, M. L. Chan, C. Messenger, and X. Fan, “Exploring the sky localization and early warning capabilities of third generation gravitational wave detectors in three-detector

- network configurations,” *Phys. Rev. D* **105** no. 4, (2022) 043010, [arXiv:2109.07389](#) [[astro-ph.IM](#)].
- [34] M. Pieroni, A. Ricciardone, and E. Barausse, “Detectability and parameter estimation of stellar origin black hole binaries with next generation gravitational wave detectors,” *Sci. Rep.* **12** no. 1, (2022) 17940, [arXiv:2203.12586](#) [[astro-ph.CO](#)].
- [35] M. Vallisneri, “Use and abuse of the Fisher information matrix in the assessment of gravitational-wave parameter-estimation prospects,” *Phys. Rev. D* **77** (2008) 042001, [arXiv:gr-qc/0703086](#).
- [36] C. L. Rodriguez, B. Farr, W. M. Farr, and I. Mandel, “Inadequacies of the Fisher Information Matrix in gravitational-wave parameter estimation,” *Phys. Rev. D* **88** no. 8, (2013) 084013, [arXiv:1308.1397](#) [[astro-ph.IM](#)].
- [37] A. H. Nitz and T. Dal Canton, “Pre-merger Localization of Compact-binary Mergers with Third-generation Observatories,” *Astrophys. J. Lett.* **917** no. 2, (2021) L27, [arXiv:2106.15259](#) [[astro-ph.HE](#)].
- [38] M. Mancarella, F. Iacovelli, S. Foffa, N. Muttoni, and M. Maggiore, “Accurate standard siren cosmology with joint gravitational-wave and γ -ray burst observations,” [arXiv:2405.02286](#) [[astro-ph.HE](#)].
- [39] G. Pratten *et al.*, “Computationally efficient models for the dominant and subdominant harmonic modes of precessing binary black holes,” *Phys. Rev. D* **103** (2021) 104056, [arXiv:2004.06503](#) [[gr-qc](#)].
- [40] S. Khan, S. Husa, M. Hannam, F. Ohme, M. Pürrer, X. Jiménez Forteza, and A. Bohé, “Frequency-domain gravitational waves from nonprecessing black-hole binaries. II. A phenomenological model for the advanced detector era,” *Phys. Rev. D* **93** (2016) 044007, [arXiv:1508.07253](#) [[gr-qc](#)].
- [41] T. Dietrich, A. Samajdar, S. Khan, N. K. Johnson-McDaniel, R. Dudi, and W. Tichy, “Improving the NRTidal model for binary neutron star systems,” *Phys. Rev. D* **100** (2019) 044003, [arXiv:1905.06011](#) [[gr-qc](#)].
- [42] L. Wade, J. D. E. Creighton, E. Ochsner, B. D. Lackey, B. F. Farr, T. B. Littenberg, and V. Raymond, “Systematic and statistical errors in a bayesian approach to the estimation of the neutron-star equation of state using advanced gravitational wave detectors,” *Phys. Rev. D* **89** (2014) 103012, [arXiv:1402.5156](#) [[gr-qc](#)].
- [43] M. Mapelli, N. Giacobbo, E. Ripamonti, and M. Spera, “The cosmic merger rate of stellar black hole binaries from the Illustris simulation,” *Mon. Not. Roy. Astron. Soc.* **472** no. 2, (2017) 2422–2435, [arXiv:1708.05722](#) [[astro-ph.GA](#)].
- [44] N. Giacobbo, M. Mapelli, and M. Spera, “Merging black hole binaries: the effects of progenitor’s metallicity, mass-loss rate and Eddington factor,” *Mon. Not. Roy. Astron. Soc.* **474** no. 3, (2018) 2959–2974, [arXiv:1711.03556](#) [[astro-ph.SR](#)].
- [45] N. Giacobbo and M. Mapelli, “The impact of electron-capture supernovae on merging double neutron stars,” *Mon. Not. Roy. Astron. Soc.* **482** no. 2, (2019) 2234–2243, [arXiv:1805.11100](#) [[astro-ph.SR](#)].
- [46] M. Mapelli, M. Spera, E. Montanari, M. Limongi, A. Chieffi, N. Giacobbo, A. Bressan, and Y. Bouffanais, “Impact of the Rotation and Compactness of Progenitors on the Mass of Black Holes,” *Astrophys. J.* **888** (2020) 76, [arXiv:1909.01371](#) [[astro-ph.HE](#)].
- [47] N. Giacobbo and M. Mapelli, “Revising natal kick prescriptions in population synthesis simulations,” [arXiv:1909.06385](#) [[astro-ph.HE](#)].
- [48] F. Santoliquido, M. Mapelli, N. Giacobbo, Y. Bouffanais, and M. C. Artale, “The cosmic merger rate density of compact objects: impact of star formation, metallicity, initial mass

- function and binary evolution,” *Mon. Not. Roy. Astron. Soc.* **502** no. 4, (2021) 4877–4889, [arXiv:2009.03911 \[astro-ph.HE\]](#).
- [49] M. Mapelli *et al.*, “Hierarchical black hole mergers in young, globular and nuclear star clusters: the effect of metallicity, spin and cluster properties,” *Mon. Not. Roy. Astron. Soc.* **505** no. 1, (2021) 339–358, [arXiv:2103.05016 \[astro-ph.HE\]](#).
- [50] M. Mapelli, Y. Bouffanais, F. Santoliquido, M. A. Sedda, and M. C. Artale, “The cosmic evolution of binary black holes in young, globular, and nuclear star clusters: rates, masses, spins, and mixing fractions,” *Mon. Not. Roy. Astron. Soc.* **511** no. 4, (2022) 5797–5816, [arXiv:2109.06222 \[astro-ph.HE\]](#).
- [51] S. Vitale and M. Evans, “Parameter estimation for binary black holes with networks of third generation gravitational-wave detectors,” *Phys. Rev. D* **95** no. 6, (2017) 064052, [arXiv:1610.06917 \[gr-qc\]](#).
- [52] S. Vitale and C. Whittle, “Characterization of binary black holes by heterogeneous gravitational-wave networks,” *Phys. Rev. D* **98** no. 2, (2018) 024029, [arXiv:1804.07866 \[gr-qc\]](#).
- [53] K. K. Y. Ng, S. Chen, B. Goncharov, U. Dupletsa, S. Borhanian, M. Branchesi, J. Harms, M. Maggiore, B. S. Sathyaprakash, and S. Vitale, “On the Single-event-based Identification of Primordial Black Hole Mergers at Cosmological Distances,” *Astrophys. J. Lett.* **931** no. 1, (2022) L12, [arXiv:2108.07276 \[astro-ph.CO\]](#).
- [54] K. K. Y. Ng *et al.*, “Measuring properties of primordial black hole mergers at cosmological distances: Effect of higher order modes in gravitational waves,” *Phys. Rev. D* **107** no. 2, (2023) 024041, [arXiv:2210.03132 \[astro-ph.CO\]](#).
- [55] S. Fairhurst, C. Mills, M. Colpi, R. Schneider, A. Sesana, A. Trinca, and R. Valiante, “Identifying heavy stellar black holes at cosmological distances with next-generation gravitational-wave observatories,” *Mon. Not. Roy. Astron. Soc.* **529** no. 3, (2024) 2116–2130, [arXiv:2310.18158 \[astro-ph.HE\]](#).
- [56] M. Mancarella, F. Iacovelli, and D. Gerosa, “Inferring, not just detecting: Metrics for high-redshift sources observed with third-generation gravitational-wave detectors,” *Phys. Rev. D* **107** no. 10, (2023) L101302, [arXiv:2303.16323 \[gr-qc\]](#).
- [57] B. Allen and J. D. Romano, “Detecting a stochastic background of gravitational radiation: Signal processing strategies and sensitivities,” *Phys. Rev. D* **59** (1999) 102001, [arXiv:gr-qc/9710117](#).
- [58] M. Maggiore, “Gravitational wave experiments and early universe cosmology,” *Phys. Rept.* **331** (2000) 283–367, [arXiv:gr-qc/9909001 \[gr-qc\]](#).
- [59] E. Thrane and J. D. Romano, “Sensitivity curves for searches for gravitational-wave backgrounds,” *Phys. Rev. D* **88** no. 12, (2013) 124032, [arXiv:1310.5300 \[astro-ph.IM\]](#).
- [60] K. Janssens, K. Martinovic, N. Christensen, P. M. Meyers, and M. Sakellariadou, “Impact of Schumann resonances on the Einstein Telescope and projections for the magnetic coupling function,” *Phys. Rev. D* **104** no. 12, (2021) 122006, [arXiv:2110.14730 \[gr-qc\]](#).
- [61] K. Janssens *et al.*, “Correlated 0.01Hz-40Hz seismic and Newtonian noise and its impact on future gravitational-wave detectors,” [arXiv:2402.17320 \[gr-qc\]](#).
- [62] M. Maggiore, *Gravitational Waves. Vol. 2: Astrophysics and Cosmology*. Oxford University Press, 2018.
- [63] C. Cutler and J. Harms, “BBO and the neutron-star-binary subtraction problem,” *Phys. Rev. D* **73** (2006) 042001, [arXiv:gr-qc/0511092](#).

- [64] J. Harms, C. Mahrtdt, M. Otto, and M. Priess, “Subtraction-noise projection in gravitational-wave detector networks,” *Phys. Rev. D* **77** (2008) 123010, [arXiv:0803.0226 \[gr-qc\]](#).
- [65] T. Regimbau, M. Evans, N. Christensen, E. Katsavounidis, B. Sathyaprakash, and S. Vitale, “Digging deeper: Observing primordial gravitational waves below the binary black hole produced stochastic background,” *Phys. Rev. Lett.* **118** no. 15, (2017) 151105, [arXiv:1611.08943 \[astro-ph.CO\]](#).
- [66] S. Sachdev, T. Regimbau, and B. S. Sathyaprakash, “Subtracting compact binary foreground sources to reveal primordial gravitational-wave backgrounds,” *Phys. Rev. D* **102** no. 2, (2020) 024051, [arXiv:2002.05365 \[gr-qc\]](#).
- [67] B. Zhou, L. Reali, E. Berti, M. Çalhşkan, C. Creque-Sarbinowski, M. Kamionkowski, and B. S. Sathyaprakash, “Subtracting Compact Binary Foregrounds to Search for Subdominant Gravitational-Wave Backgrounds in Next-Generation Ground-Based Observatories,” [arXiv:2209.01310 \[gr-qc\]](#).
- [68] M. Maggiore, *Gravitational Waves. Vol. 1: Theory and Experiments*. Oxford University Press, 2007.
- [69] R. Brustein, M. Gasperini, M. Giovannini, and G. Veneziano, “Relic gravitational waves from string cosmology,” *Phys. Lett. B* **361** (1995) 45–51, [arXiv:hep-th/9507017](#).
- [70] A. Buonanno, M. Maggiore, and C. Ungarelli, “Spectrum of relic gravitational waves in string cosmology,” *Phys. Rev. D* **55** (1997) 3330–3336, [arXiv:gr-qc/9605072](#).
- [71] I. Ben-Dayan, G. Calcagni, M. Gasperini, A. Mazumdar, E. Pavone, U. Thattarampilly, and A. Verma, “Gravitational-wave background in bouncing models from semi-classical, quantum and string gravity,” [arXiv:2406.13521 \[gr-qc\]](#).